

The CFHT Legacy Survey: stacked images and catalogs

Stephen. D. J. Gwyn

Canadian Astronomical Data Centre, Herzberg Institute of Astrophysics, 5071 West Saanich Road, Victoria, British Columbia, Canada V9E 2E7

Stephen.Gwyn@nrc-cnrc.gc.ca

ABSTRACT

This paper describes the image stacks and catalogs of the CFHT Legacy Survey produced using the MegaPipe data pipeline at the Canadian Astronomy Data Centre. The Legacy Survey is divided into two parts: The Deep Survey consists of 4 fields each of 1 square degree, with magnitude limits of $u = 27.5$, $g = 27.9$, $r = 27.7$, $i = 27.4$, and $z = 26.2$, and contains 1.6×10^6 sources. The Wide Survey consists of 171 square degree pointings split over 4 fields, with magnitude limits of $u = 26.0$, $g = 26.5$, $r = 25.9$, $i = 25.7$, and $z = 24.6$, and contains 3×10^7 sources. This paper describes the calibration, image stacking and catalog generation process. The images and catalogs are available on the web through several interfaces: normal image and text file catalog downloads, a “Google Sky” interface, an image cutout service, and a catalog database query service.

Subject headings: methods: data analysis, astronomical data bases: miscellaneous, astrometry, techniques: photometric

1. INTRODUCTION

The Canada France Hawaii Telescope Legacy Survey (CFHTLS) consisted of three surveys: The Deep Survey imaged 4 square degrees; the primary goal was to measure cosmological parameters using Type Ia supernovae as standard candles. This portion of the CFHTLS is also known as the Super Nova Legacy Survey (Astier et al. 2006, SNLS). The Wide survey covered a wider area (150 square degrees) to shallower depth. Weak lensing and large scale structure studies were the primary science goals. The Very Wide portion of the survey covered the ecliptic plane and was designed to study Kuiper Belt Objects. It was cancelled mid-way through the project but has become the Canada-France Ecliptic Plane Survey (Kavelaars et al. 2009, CFEPS).

Interestingly, image stacks are secondary to the main science goals of the CFHTLS. The main reason for the Deep Fields is supernova cosmology. The supernovae are discovered using stacks generated on a nightly basis. Deeper stacks are generated but only as a reference for difference imaging. Similarly, the main science driver of the Wide fields is weak lensing. The actual weak lensing measurements are done on individual images in order to accurately quantify the PSF. The value of the Very Wide survey, which was looking for moving objects, is also in the individual images.

Now that the primary science goals of the CFHTLS are well in hand, the archival data becomes important. Creating stacks and catalogs greatly increases the usefulness of archival MegaCam data. The official CFHTLS stacks are being produced by Terapix at the Institut d’Astronomie de Paris. So far, these stacks have been marked by long production delays and poor calibration quality. The photometric accuracy is generally poor, often as bad as 0.1 to 0.2 mags. The lack of internal astrometric accuracy makes measuring colors difficult, and precludes any hope of measuring proper motions over the course of the survey. The latest stacks (Goranova et al. 2009, T0006) will be public soon. The final version is still in preparation.

The SNLS produced image stacks as part of the supernovae pipeline. These stacks have also been used for other science purposes, such as studying dwarf galaxy clustering (Carlberg et al. 2009). However the stacks are only available to the SNLS team.

The CFHTLS Archive Research Survey (Erben et al. 2009, CARS) has also produced stacks. So far, only 37 square degrees have been published. The stacks are available by request, but are not generally accessible.

MegaPipe (Gwyn 2008) has been used to process over 2000 square degrees of MegaCam imaging over the last four years. Twice a year it goes through the CFHT archive at the CADC, determines which images are worth combining, computes accurate astrometric/photometric calibrations, stacks the images, and makes the stacked images to the astronomical community. In addition, it is used process PI data (on request) and to process data from large surveys such as the Next Generation Virgo Survey (Ferrarese et al. in preparation)

This paper describes image stacks and catalogs of the CFHTLS Deep and Wide surveys generated by the MegaPipe image processing pipeline. It presents the astrometric and photometric calibration, the image stacking and catalog generation, and quality control. This paper outlines the various web applications that astronomers can use to download the data. This paper however does not describe the stacking of the Very Wide data; everything worth stacking was stacked as part of regular semi-annual MegaPipe processing.

Some of the methods presented in this paper have already been described in the main MegaPipe paper (Gwyn 2008). For completeness, this paper describes these methods again (usually in less detail), but more emphasis is placed on methods that are specific to the CFHTLS stack generation and quality control.

The AB magnitude (Oke 1974) system is used throughout this paper.

2. FIELD LOCATIONS

The layout and positions of the Deep fields are shown in Figure 1. The figure shows the Deep fields themselves as red outlines, with green outlines denoting overlapping MegaCam imaging. The D1 and D3 fields overlap the corresponding Wide fields and the D2 overlaps the COSMOS (Scoville et al. 2007) u^* -band imaging, as shown. The grey lines and hashed areas show the positions of the Sloan Digital Sky Survey (Abazajian et al. 2009, SDSS) swaths; the D2 and D3 lie within the SDSS.

The D1 field lies within the XMM-LSS (Chiappetti et al. 2005) and VVDS (McCracken et al. 2003) fields. Surveys at other wavelengths also overlap: near-infrared (Iovino et al. 2005), infrared (Walcher et al. 2008), and radio (Bondi et al. 2003). In addition, there is a considerable amount of spectroscopy (Le Fèvre et al. 2005)

The D2 field lies within the the COSMOS survey. There are X-ray (Hasinger et al. 2007), UV (Zamojski et al. 2007), infrared (Sanders et al. 2007), near IR (Capak et al. 2007), and radio (Schinnerer et al. 2007) data available. In addition, the zCOSMOS survey (Lilly et al. 2007) provides spectroscopic coverage.

The D3 field overlaps the Groth strip. It is the site of several previous surveys, including the CFRS (Lilly et al. 1995) and a LBG survey (Steidel et al. 2003). The ongoing AEGIS also survey overlaps the D3 (Davis et al. 2007). It includes HST imaging, X-ray (Laird et al. 2009), UV data from GALEX near-IR (Bundy et al. 2006) and infrared data from Spitzer, as well as several thousand galaxy spectra.

The layout and positions of the Wide fields are shown in Figures 2, 3, 4, and 5. Again, the pointings are shown in red and the grey lines and hashed areas show the positions of the SDSS swaths. Some pointings of all four Wide fields overlap the SDSS. The W1 and W3 overlap the D1 and D3 respectively. The W4 lies on the special area SA22 which is the location of the VVDS 22h field as well as one of the UKIDSS DXS fields (Lawrence et al. 2007).

3. INPUT IMAGE SELECTION

The images were selected from the CFHT archive at the Canadian Astronomy Data Centre. All images with centers within 0.05 degrees of the nominal pointing centers were included. For the most part these are CFHTLS images, however this also includes a number of public images from other programs. The COSMOS field consists of 4 MegaCam pointings arranged around the D2 field, and centered on it. The u^* -band images from the COSMOS program were included. Each of these images covers about a quarter of the D2 field. Images taken in the new I filter were not included in the Deep field stacks. The complete list of CFHT exposures which were included in the stacks is available on-line ¹.

3.1. Input Image Quality Control

The images were checked in a number of ways before being included in the stacks. SExtractor was run on each image. The stellar locus was identified automatically. The properties of objects in the stellar locus were used to set rejection criteria.

The image quality (ie, seeing) was measured. If the seeing was worse than 1.5", the image was rejected. Figure 6 shows the distribution of seeing for the CFHTLS input images split by survey and filter.

In addition, if the PSF is noticeably trailed (due to poor tracking), the image was rejected. If a and b are the semi-major and semi-minor axes of sources in the stellar locus, the asymmetry index, A , is given by

$$A = 1 - b/a \tag{1}$$

The average of the this index over each field, \bar{A} , is always slightly greater than 0 due to the optical aberrations in the MegaPrime optics. This index is crude, but is more than sufficient to rejected trailed images. Images with an average asymmetry index $\bar{A} > 0.2$ are noticeably trailed and were rejected.

Images taken in conditions of poor transparency were also rejected. If the measured zero-point was more than 1 magnitude below the nominal value, the image was rejected.

Finally, a subsection of one chip of each image was scrutinized by eye for other abnormalities. For example, one image flaw which cannot be detected automatically is a discrete jump in telescope position during the exposure. In this case, each source is doubled (and

¹<http://www.cadc.hia.nrc.gc.ca/community/CFHTLS-SG/docs/cfhtlsinput.html>

bright stars will leave a trail between the two image) but the PSF will stay the same. This is immediately obvious to eye, but hard to detect automatically.

3.2. Best Seeing Image Selection

Two versions of the Deep field stacks were produced: the “full” stacks and the “best seeing” stacks. This section describes how the images that went into the “best seeing” images were selected.

When making “best seeing” stacks, one must decide how many input images to include and how many to throw away. There is trade-off between limiting magnitude and image quality (IQ). As one includes more images with increasingly bad image quality, the output image quality degrades while the depth increases.

Quantitatively, the IQ of a stack of N images is very well estimated by the median of the IQ of its input images, i.e., the IQ of input image $N/2$. To estimate the limiting magnitude, two assumptions were made: 1) the effects of IQ on depth are not important (not quite true); and 2) all the input images have the same exposure time (for the CFHTLS Deep Fields, quite true). In this simplified case, the limiting magnitude of a stack of N images goes approximately as $1.25 \log_{10} N$.

These two measures were applied to the input images of the CFHTLS Deep fields. The images were sorted in order of image quality: best seeing first, worst seeing last. As the number of input images increases, the image quality of the stack will get worse, but the limiting magnitude will get deeper. The results are shown in the grid of plots of Figure 7. The expected image quality is plotted against expected limiting magnitude for each the 5 filters and 4 deep fields. The black lines show both IQ and limiting magnitude increasing with number of images. The red points show the locus of the “full” stacks.

It can be seen that while the median of the image quality of the input images is an excellent predictor of the IQ of the output stacks, the limiting magnitude prediction is less accurate. Deviations of several tenth of a magnitude from the prediction are not uncommon. This not surprising, given the simplifying assumptions.

The question becomes: is there a “sweet spot” on the graphs, where an improvement in image quality comes at only a small cost in limiting magnitude? Some of the graphs exhibit kinks where the slope of the line changes. Obviously, it is better to be at or slightly below these kinks. Ideally all the output images would have the same IQ, to increase the accuracy of matched aperture photometry.

Instead of picking a single threshold (for example stacking the best 25% of the images, or stacking only images with $\text{IQ}=0.7''$ or better), images were included to produce a desired output image quality. This is possible because, as shown by the red dots on the Figure 7, the median input IQ is an excellent predictor of the output IQ. Therefore, when choosing input images, one first sorts the images by increasing IQ. Then one goes down the ordered list until an input image with the target IQ is found, and then selects twice that number of images. For example, if one wants a $0.65''$ seeing stack, and there are 41 images with seeing better than $0.65''$, one should stack the best 82 images.

The chosen target image quality was $0.65''$ for the $g'r'i'z'$ filters and $0.8''$ for the u^* filter. Decreasing the seeing below 0.8 becomes rapidly prohibitive for the u^* -band. Similarly, the z' - and particular the g' -band depths decrease rapidly if the target IQ is decreased even slightly. The u^* -band target is different than the other bands because targeting $\text{IQ}=0.65''$ would include no images, and targeting $\text{IQ}=0.8''$ in the other bands would improve the seeing only slightly relative to the "full" stacks.

These criteria were applied to the input images of the CFHTLS Deep Fields and the chosen images were stacked. The resulting image quality and limiting magnitudes are plotted as blue dots on Figure 7. The image quality is consistently on (or very slightly below) the prediction. The limiting magnitudes are usually better than predicted, since the prediction relies on the (not completely correct) assumption that IQ does not affect depth.

3.3. Elixir Preprocessing

The Elixir pipeline (Magnier & Cuillandre 2004) at CFHT processed each MegaCam image. The CCD images were detrended: the bias was subtracted and the flat field response was corrected. Elixir also removed the fringing for the i' and z' bands. It applied a relative flux calibration across the camera field of view. When possible, a photometric zero-point for each exposure was derived from standard stars. Elixir also provided an approximate astrometric solution usually good to about $0.5\text{-}1.0''$.

4. ASTROMETRIC CALIBRATION

The astrometric calibration consisted of generating a catalog of sources from the input MegaCam images, retrieving an astrometric reference catalog, and determining the mapping between the two. The mapping was then expressed in terms the FITS WCS (World Coordinate System) parameters. This mapping was then used by SWarp in the resampling phase

of the stacking procedure.

4.1. Source Catalog Generation

SExtractor (Bertin & Arnouts 1996) was used to generate the image source catalog. The source catalog was limited to brighter sources with well defined centres. The parameters were set such that sources must have 5 continuous pixels 5σ above the sky level in order to count as a detection. (DETECT_MINAREA=5 and DETECT_THRESH=5 in SExtractor parlance). The catalog was cleaned. Cosmic rays were rejected by removing sources which are more compact than stars as measured by their half-light radius. Extended sources were identified and rejected as those sources whose Kron magnitudes were more than 2 magnitudes greater than their $1.5''$ radius magnitudes.

4.2. Reference Catalogs

A bootstrapping series of astrometric reference catalogs were used. The Naval Observatory Merged Astrometric Dataset (Zacharias et al. 2004, NOMAD) was used as the first external astrometric catalog. Where available, the SDSS DR7 (Abazajian et al. 2009) was used to refine the astrometry. The final reference catalog was generated from a subset of the CFHTLS images themselves. For the Deep fields a subset of the images whose centers were the furthest away from field center were used. For the D2 field, some archival COSMOS images were included; for the D3, some W3 images were included. Only i' -band images were used. For the Wide fields, images from the main pointings were supplemented with images from the “pre-imaging” survey. Here, r' band images were used. Each of these images were calibrated using the NOMAD/SDSS astrometric solutions. Source catalogs were generated for each images with SExtractor; the catalogs were cleaned as noted in Section 4.1 with a further magnitude cut at $\text{mag}=23.$. The (x, y) positions were converted to (RA, Dec) using the astrometric solutions. The catalogs for a given survey and field were then merged, forming an final reference catalog for each field. These internal catalogs have smaller astrometric residuals and a higher source density than the external catalogs. Using these internal catalogs left the external astrometric accuracy unchanged (or improved very slightly) but dramatically improved the internal astrometric accuracy.

4.3. Mapping

The first step of the mapping was the initial matching up of the observed catalogs (section 4.1) to the reference catalogs (section 4.2). For the matching, each CCD of the mosaic was treated independently. The (x, y) coordinates of the observed catalog were converted to (RA, Dec) using the initial Elixir WCS. The catalogs were shifted in RA and Dec with respect to one another until the best match between the two catalogs was found. This simple up-down/left-right shift method was found to be sufficient. More complex methods such as triangle matching or Fourier transform methods were not necessary since the plate scale and image orientation were known beforehand. If there was no good match for a particular CCD (for example, when the initial Elixir WCS unusually erroneous), its WCS was replaced with a default WCS and the matching procedure was restarted. Once the matching was complete, the astrometric fitting could begin. The initial matching was always done with the NOMAD catalog; the higher source density of the SDSS and the internal catalogs would have made matching prohibitively slow. Typically 20 to 50 sources per CCD were found with this initial matching.

Once the initial match was complete, the first astrometric solution was determined. Using this astrometric solution, the matching was restarted, this time with tighter constraints on what constituted a good match between a observed source and an source in the reference catalogs. This procedure was repeated several times, steadily shrinking the matching radius from 8 arcseconds to 0.5 arcseconds. The order of astrometric solution increased from a linear fit in the first iteration to a 3rd order solution by the last. This match/map/repeat procedure was done for each CCD individually.

The final astrometric mapping for each image was determined on the scale of the whole mosaic, all 36 CCDs at once. This final mapping consists of a linear mapping for each CCD: shift and skew for each axis. In terms of FITS WCS keywords, this corresponds to the CRVAL/CRPIX keywords and the CD matrix. The radial distortion correction is modeled as:

$$R = r(1 + a_2r^2 + a_4r^4), \quad (2)$$

where R is the true radius and r is the measured radius. This equation is analogous to equation 3 of Chiu (1976) and the equation in Section 3.1 of Cuillandre et al. (1996). Thus, only 2 parameters were used to describe the distortion for the whole mosaic. In other systems, a second or third order function is needed to describe the distortion, requiring up to 20 parameters per CCD, or a total of 720 parameters per mosaic. The best values of a_2 and a_4 were found through a crude but robust mapping of parameter space. Once determined, the astrometric mapping described by the values a_2 and a_4 was re-expressed in terms of the FITS WCS PVn_n keywords (Calabretta et al. 2004), so as to be understood by SWarp.

5. PHOTOMETRIC CALIBRATION

5.1. Using SDSS

The SDSS DR7 (Abazajian et al. 2009) served as the basis of the photometric calibration. The Sloan *ugriz* filters are not identical to the MegaCam filters, as shown in Figure 8. The color terms between the two filter sets can be described by the following equations:

$$\begin{aligned}
 u^* &= u_{SDSS} - 0.211 \times (u_{SDSS} - g_{SDSS}) \\
 g' &= g_{SDSS} - 0.155 \times (g_{SDSS} - r_{SDSS}) \\
 r' &= r_{SDSS} - 0.030 \times (r_{SDSS} - i_{SDSS}) \\
 i' &= i_{SDSS} - 0.102 \times (r_{SDSS} - i_{SDSS}) \\
 z' &= z_{SDSS} + 0.036 \times (i_{SDSS} - z_{SDSS})
 \end{aligned}
 \tag{3}$$

after Regnault et al. (2009).

All images lying in the SDSS were directly calibrated without referring to other standard stars such as Smith et al. (2002) standards. The systematics in the SDSS photometry are about 0.02 magnitudes (Ivezić et al. 2004) The presence of at least 1000 usable sources in each square degree reduced the random error to effectively zero. It was possible to calibrate the CCDs of the mosaic individually with about 30 standards in each. For each MegaCam image, the corresponding catalog (in instrumental magnitudes) was matched to the to SDSS catalog for that patch of sky. The difference between the instrumental MegaCam magnitudes and the SDSS magnitudes gave the zero-point for that exposure or that CCD. The zero-point was determined by median.

There are about 10^4 SDSS sources per square degree, but when one cuts by stellarity and magnitude this number drops to around 1000. Only stars were used since the above color terms are more appropriate to stars than galaxies. Only objects with $17 < \text{mag} < 20$ were used; the brighter objects are usually saturated in the MegaCam image and including the fainter objects tends to only increase the noise in the median. This process could be used any night; it was not necessary for the night to be photometric. The D2, D3, and the W3 were calibrated in this manner.

5.2. Using Elixir

For pointings outside the SDSS, the Elixir photometric keywords were used, with modifications. The Elixir zero-points were compared to those determined from the SDSS using the procedure above for a large number of archival MegaCam images. There are systematic

offsets between the two sets of zero-points, particularly for the u^* -band. These offsets show variations with epoch, which are caused by modifications to Elixir pipeline (Cuillandre, private communication). There are also differential offsets between the CCDs of a single image. For MegaPipe, the offsets are applied from the Elixir zero-points to bring them in line with the SDSS zero-points.

The differential offsets are the offsets between different CCDs of a single MegaCam image, regardless of whether the image was taken under photometric conditions or not. Ideally, the photometric zero-point should be the same across the MegaCam field. In practice, differences exist. To investigate the differential zero-point offsets, the MegaCam archive was searched for images matching the following criteria:

- Each image must have an exposure time greater than 60 seconds
- Each image must lie within the SDSS
- No two images from the same camera run should lie within 0.3 degrees of each other.

The last condition is to ensure that the isolated patches of bad SDSS photometry don't affect the final result.

Each of the 12 000 images matching these criteria was astrometrically calibrated using the standard MegaPipe pipeline. The photometric zero-points were computed separately for each CCD. The difference between the individual zero-points and the average of all the zero-points was computed. Since the images were not necessarily taken under photometric conditions, the Elixir zero-point may or may not be valid, and therefore was ignored at this stage. The old i' filter (I.MP9701) and the new i' filter (I.MP9702) were treated separately.

The resulting differential zero-point measurements were aggregated by filter and camera run ID (=CRUNID). For each of the CCDs, a median photometric zero-point offset was computed for each filter/CRUNID combination. The individual and median zero-point offsets were plotted. Two examples are shown in Figure 9. In these plots the black lines show the individual zero-point offsets (SDSS-Elixir) as a function of CCD number. The superimposed red line shows the median zero-point offsets. There is some scatter about the median, indicated by the black lines and by the error bars (1 sigma). The pattern of offsets by CCD number reflects the mostly radial pattern noted by Regnault et al. (2009). The amplitude of the pattern varies with filter, but also over time. There is considerable variation in the differential zero-point offsets. For some runs the differential offsets are quite small, as shown by the upper panel of Figure 9. For others it is substantial, (0.08 mags or greater), as shown in the lower panel. Going through the plots sequentially, one sees definite changes

over time. Further, at least in some cases, the amplitude of the offsets is large enough to warrant correction.

Zero-point corrections were determined for every CRUNID and filter combination. These corrections were then applied to every CFHTLS image which was not calibrated using the SDSS.

The next step was to measure the offsets of the MegaPipe mosaic as a whole with respect to the SDSS. To measure this for a given image, the Elixir zero-point determined from the header keywords was compared to the zero-point determined by comparing the instrumental magnitudes of stars in the images to the magnitudes in the the SDSS. As before, the MegaCam archive was searched for all suitable images. In this case, the criteria were slightly different. In order for the Elixir zero-point to be valid, the night must have been photometric. Whether or not a given night was photometric was determined using the SkyProbe (Cuillandre et al. 2002) plots. The patches of bad SDSS photometry are small relative to the size of the MegaPrime field of view so the requirement that all the pointings must be different was relaxed. The new criteria were then:

- Each image must have an exposure time greater than 60 secs
- Each image must lie within the SDSS
- The night must be photometric.

For each image, the average difference between the SDSS and Elixir zero-point over all the CCDs was measured. SExtractor was run on the image with `MAG_ZEROPOINT=0`. The resulting catalog was astrometrically calibrated using the standard MegaPipe system. The relevant part of the SDSS catalog was retrieved from the web. The SDSS magnitudes were converted to MegaCam magnitudes using the transformations described earlier.

The image catalog was matched to the SDSS catalog. The difference between the instrumental magnitudes and the SDSS magnitudes (transformed into the MegaCam filter system using Equation 3) yields the SDSS photometric zero-point. The Elixir zero-point ZP_{Elixir} was calculated from the MegaCam image header keywords as follows:

$$ZP_{\text{Elixir}} = \text{PHOT_C} + \text{PHOT_K} \times (\text{AIRMASS} - 1) + 2.5 \times \log_{10}(\text{EXPTIME}) \quad (4)$$

where `PHOT_C` is the nightly instrumental zero point determined by Elixir, `PHOT_K` is the airmass coefficient, `AIRMASS` denotes the airmass, and `EXPTIME` is the exposure time.

The differential offset described above were also applied to the Elixir zero-points. Note that because differential offsets average to 0 over the whole mosaic (by design), applying

these offsets only reduces the scatter of the individual CCD zero-points about the average zero-point, but does not change the value of the average zero-point.

The zero-point differences were then aggregated by filter and CRUNID. The median zero-point difference was computed, as well as the standard deviation about this median. For some filter/CRUNID combinations, no data was taken on photometric nights. For other combinations, data was available for multiple photometric nights during a single run. In a number of cases, there was variation in the zero-point difference between two apparently photometric nights of the same run. The zero-point differences might be stable within a single night, but differences were found from night to night. In addition, there were occasionally variations in the zero-point differences within a single night, indicating that the night was not photometric.

The zero-point differences for the filter/CRUNID combinations were sorted into three categories, labeled “No info”, “Excellent”, and “Marginal” as follows:

- No info: No data was taken on photometric nights during this camera run with this filter.
- Excellent: Data was taken on a least two photometric nights during this camera run, and at least 6 images were taken on those nights, and the scatter about the median zero-point difference is less than 0.02 magnitudes.
- Marginal: There is some data, but it doesn’t meet the criteria outlined above. Either data was not taken on more than one night, or less than 6 images were taken, or the scatter is large.

Figure 10 shows the zero-point history of MegaCam for the $u^*g'r'i'z'$ filters. Each point represents a single CRUNID. The “Excellent” cases are shown in red. The “Marginal” case are shown in black. The “No info” cases are not shown. The Elixir zero-point is not always consistent with the SDSS zero-point. The amplitude of the variation is typically about 0.05 magnitudes, except for the u^* -band, for which the amplitude is greater than 0.2 magnitudes.

Thus, two sets of corrections were applied to the Elixir zero-points: A differential correction was applied to each CCD within the mosaic and a global correction was applied the mosaic as a whole. Both sets of corrections were applied as a function of CRUNID. Applying these corrections greatly increased the consistency of the photometry, as discussed in Section 8.2

5.3. Using Overlapping Images

Some of the CFHTLS data neither lie in the SDSS nor were taken on a photometric night. These data can not be photometrically calibrated by either of the preceding methods. However, if such an image overlaps another which can be calibrated by one the preceding methods, it in turn can be calibrated.

For the Deep fields, this was fairly straightforward. Since all the images in a field lie at same position, in-field photometric standards using images taken on photometric nights were established. Those standards were then used to calibrate all the data for that field. In fact, the self-consistency of the photometry was used to determine which nights were photometric. The two Deep fields which do not lie in the SDSS, the D1 and the D4, were calibrated in this manner. The initial photometry was computed for each image using the Elixir zero-points. Catalogs were generated for each image based on these zero-points and the catalogs were cross-referenced to each other to determine image-to-image variations in photometry. The photometric consistency was checked over each night. Any night showing large variation in photometry from image to image was deemed non-photometric. (Interestingly, some of these nights appear completely photometric based on the SkyProbe measurements.) While the presence of large variation indicates that the night was not photometric, the absence of such variations does not guarantee that the night was photometric. The photometric catalogs on the apparently photometric nights were compared over the run of the survey. Again, if the photometry for a given night was not consistent with that of other nights, it was flagged as non-photometric. In the end, a minimum of 5 nights per filter and per field were identified as both photometric and consistent. The images from these nights were stacked and a catalog generated from the resulting image. This catalog became the photometric reference for that field and filter.

A similar method was used for the Wide fields. The pointings within a field overlap at the edges, allowing photometric comparisons. Each filter was processed separately. First, the photometry was homogenized within each pointing. In the simplest case, all the images within a pointing could be directly calibrated using either the (corrected) Elixir zero-points or the SDSS. These pointings were flagged as “probably photometric”. If only some of the images of a pointing could be directly calibrated, these images were used as reference for the others. These pointings were also flagged as “probably photometric”. If none of the images could be calibrated directly, one of the images was used as a photometric reference for the others. The photometry of the images in this pointing would be self-consistent within itself, but probably not with adjacent pointings. These pointings were flagged as “not photometric”.

Next, the photometric consistency between pointings was checked. Consistency here

means a systematic zero-point difference of less than 0.03 magnitudes. If a pointing previously flagged “probably photometric” was found to be inconsistent with any other “probably photometric” or “definitely photometric” pointing, then its status was downgraded to “not photometric”. On the other hand, if a pointing was consistent with at least two other adjacent pointings its status was upgraded to “definitely photometric”.

Having identified the “definitely photometric” pointings, the next step was to calibrate adjacent pointings. There are typically a few hundred stars in the overlap region between two adjacent pointings. Only pointings which overlap along an edge were calibrated in this manner, not pointings which only overlap at the corners. The random error associated with transferring the zero-point in this manner is typically 0.05 mags per star. When 300 stars are used, the random error drops to below 0.002 mags. Once a new pointing was calibrated by overlap, it was checked for consistency with previously calibrated pointings. If it was consistent, it was flagged as “definitely photometric” and used to calibrate other adjacent pointings. Eventually all pointings in a field were calibrated. (The procedure bore some similarity to the game “Minesweeper”.) In principle transferring the zero-point in this manner could cause an increase in photometric zero-point error as the number of transfers increases. In practice all pointings were at most 2 steps away from a “definitely photometric” pointing. The W1, W2 and W4 fields were calibrated in this manner. As a check, the W3, which lies in the SDSS, was also calibrated in this manner. The zero-points thus derived were found to be consistent with the zero-points derived from the SDSS to within 0.01 mags RMS.

6. IMAGE STACKING

The calibrated images were resampled and coadded using the program **SWarp** (Bertin 2004). **SWarp** removed the sky background from each image so that its sky level was 0. It scaled each image according to the photometric calibration described in Section 5. **SWarp** then resampled the pixels of each input image to remove the geometric distortion measured in Section 4 and placed them in the output pixel grid, which is an undistorted tangent plane projection. A “Lanczos-3” interpolation kernel was used as discussed in Section 5.6.1 of Bertin (2004). The values of the flux-scaled, resampled pixels for each image were then combined into the output image by taking a median. A median is noisier than an average, but rejects image defects such as cosmic rays. The loss in depth is small (about 0.1 magnitudes). The optimum would be some sort of artificial skepticism method (Setson 1989), but this is not yet an option in **SWarp**.

The input images were weighted with mask images provided as part of the Elixir pro-

cessing. The mask images had the value 1 for good data and 0 for pixels with known image defects. An inverse variance weight map was produced along with each output image. This could be used as an input when running SExtractor on the stack.

The resulting stacks measure about 20000 pixels by 20000 pixels or about 1 degree by 1 degree and are about 1.7 Gb in size. They have a sky level of 0 counts. They are scaled to have a photometric zero-point of 30.000 in AB magnitudes - that is to say, for each source:

$$AB_{magnitude} = -2.5 \times \log_{10}(\text{counts in ADU}) + 30.000 \quad (5)$$

7. CATALOG GENERATION

7.1. Single Image Catalogs

SExtractor was run on each image to produce a catalog. The images were filtered before detection. The detection criteria were that 3 adjacent pixels had to have flux levels 1σ above the background. The SExtractor’s deblend contrast parameter was set to 0.002. Table 4 shows the relevant SExtractor detection parameters. The inverse variance weight maps described in the previous section were used. The resulting catalogs, one per pointing and filter, are available on the web as described in Section 9.

7.2. Catalog Masking

The individual catalogs were masked to identify areas where the detection and photometric measurements of sources may be compromised. These areas include areas around bright stars, diffraction and bleed spikes from the brightest stars and satellite/meteor trails. Also, in some cases the dither pattern of the input images was insufficient to provide uniform depth across the pointing. An automatic detection method was used to find the bright stars and the diffraction/bleed spikes. This was supplemented with laborious hand masking.

The areas around bright stars were masked. The Guide Star Catalog 2 (Lasker et al. 2008) was queried for the position and magnitude of stars brighter than 15^{th} magnitude. The stars were masked with a circular mask covering the core of the star and a cross-shaped area covering the diffraction spikes. The size of the mask scaled with the brightness of the star. The top left panel of Figure 11 shows an example. Stars brighter than 13^{th} magnitude often produce bleed trails in the images extending along the y-axis of the CCDs. The masking algorithm followed the bleed trails until they blended into the sky background, extending the cross part of the stellar masks in the vertical direction. The top right panel of Figure 11

shows an example.

Stars brighter than 9^{th} magnitude also produce a visible pupil image. These halos have a radius of about 1100 MegaCam pixels (approximately 3.5 arcminutes). The center of the halos are offset from the star that created it towards the center of the MegaCam field; the size of the offset is 0.022 times the distance of the star to the center of the field, as noted in Section 3.4 of Erben et al. (2009). The bottom left panel of Figure 11 shows an example of a pupil mask.

In addition, meteor trail residuals were masked. Since meteor trails only show up in one image, and since a median is used to combine the images, these are mostly removed during the stacking process, leaving at most some residual noise. However, in some places (the gaps between CCDs of the MegaCam mosaic and over bad columns) less than the full number of input images was available, and the meteor trails were visible in the output image. The trail masking method described in Section 3.4, item 3. of Erben et al. (2009) was attempted. However as noted in that section, it is not 100% reliable. Additional hand masking of meteor trails was required. The bottom right panel of Figure 11 shows an example of meteor trail masking near the edge of a mosaic.

Masks were generated for each image of the survey. The masks were checked by eye and minor modifications made. The masks are available for download as ds9 region files².

7.3. Merged Catalogs

To increase the user-friendliness of the catalogs, the individual catalogs were merged. Each merged catalog contains measurements in all 5 of the $u^*g'r'i'z'$ MegaCam filters and covers an entire survey (either the Wide or the Deep).

Separate catalogs were generated using each of the 5 bands as a reference/detection image. Thus there is an u^* -selected, g' -selected, r' -selected, i' -selected and z' -selected catalog for each survey each suited to different science goals. (e.g. i' -selected for general galaxy population studies, z' -selected if you are looking for i' -band dropouts, g' -band for galactic stars, etc.). Although the catalogs are selected in a single filter, measurements are made in all 5 filters for each catalog, removing the need to consult multiple catalogs. There are thus a total of $5 \times 2 = 10$ separate catalogs, each complete in itself, but with different detection characteristics.

²<http://www.cadc-ccda.hia-ihp.nrc-cnrc.gc.ca/community/CFHTLS-SG/docs/catdoc.html#mask>

The procedure to produce the merged catalogs is:

- Individual catalog generation: SExtractor is run in double-image mode on the individual images.
- Catalog masking: Areas where photometric measurements and detections may be compromised are masked as described in section 7.2.
- Catalog merging: The masked catalogs for each pointing are combined and redundant sources (ones which appear in more than one individual catalogs) are removed.

Before settling on this procedure, A number of other methods were considered and ultimately rejected:

Instead of generating catalogs pointing-by-pointing and then merging the catalogs, one could SWarp together all the images for each Wide field into a single enormous image and run SExtractor on that image. This has the advantage of eliminating the catalog merging step, which involves a fair amount of book-keeping. The disadvantage is that these images are unwieldy. They would measure up to 140 000 pixels across and be 100 Gb in size. While it may be possible (although difficult) to run SExtractor on such images, one cannot distribute such images over the web. Users would be presented with catalogs for which they cannot view the source image.

Instead of generating separate catalog for each filter, one could build some sort of master image containing flux from each band, for example a χ^2 image. One could then use SExtractor in double-image mode with the master image as a detection image. This has the advantage of simplicity: it produces a single catalog. However, the 5 bands are not even in depth. The z-band in particular is much noisier than the other 4. While adding the bands together produces a deeper image in theory (you now have photons from all wavelengths), in practice it is also noisier. Leaving out the noisier bands (u^*z') means that the resulting catalog is no longer suitable for all purposes.

Instead of publishing a separate catalog for each filter, one could merge the 5 catalogs into one. One could cross-identify sources common to different catalogs and merge their entries into a single entry. This again has the advantage of producing a single catalog rather than several, and (if done correctly) eliminates the disadvantages of the previous master-image method. The trick, of course, is accurately and reliably cross-identifying the sources between filters. For bright, well separated sources this is easy. The MegaPipe images are registered to very high accuracy, making cross-identification by position fairly accurate. However the image quality and depth varies between different filters; objects that appear

as single source in one filter may appear as two sources in another filter. Even if the cross-identification can be done correctly, the bookkeeping is non-trivial. That being said, it has worked successfully for the SDSS and this option may be explored in the future.

In short, the easiest way to make a clean catalog is to:

- merge the different pointings at the catalog level rather than at the image level
- not to merge the catalogs for different filters but to generate multiple catalogs, one per filter.

7.3.1. Individual Catalog Generation

SExtractor was run on the 5 images from each pointing using “double-image mode”. In this mode, the detection of objects is done in one image (the reference image) and photometric (and other) measurements are done in the other (the measurement image). All possible image combinations were run for a total of 25 catalogs per pointing (5 possible detection images \times 5 possible measurement images).

7.3.2. Catalog merging

The final step was to merge the catalogs. For the Deep fields, which do not overlap, the catalogs for the individual fields were simply concatenated. The pointings of the Wide fields however, overlap slightly. Simply concatenating the individual catalogs would lead to many sources being double-counted.

There are a few methods that can be used to avoid double-counting. One is to divide the Wide fields with a grid corresponding to the boundaries between pointings. Sources detected inside the boundary of a pointing are added to the catalog. Sources outside the boundary are ignored since they will presumably be detected in the adjacent pointing. The problem with this method is that if there is any uncertainty in the position of an object near a boundary it may be double counted (position errors may shift it over the boundary into both adjacent pointings) or be missed entirely (position errors may shift it out of both pointings).

The other extreme is to include all objects from all the catalogs and then run a filter to determine which objects have been duplicated. Sources which come from different catalogs but lie within some small radius of each other are probably the same source; one then eliminates the redundant source. The problem with this method is that the chance of two

truly different sources lying near each other may be non-negligible, as shown in Figure 12. This figure shows $F_1(\theta)$, the probability of a source having at least one neighbour, as a function of angular separation, θ . At large angles, the chance of having a neighbouring source approaches unity. The red and blue solid lines show the results as measured from the Deep and Wide survey respectively. The measured fraction drops sharply as θ drops below 1 arcsecond. This is because sources in close proximity are increasingly unlikely to be properly deblended. The dashed lines show the theoretical nearest neighbour fractions, assuming sources are distributed completely randomly (ignoring any galaxy clustering). Sources in the Deep fields are more likely to have a neighbour simply because the Deep fields, extending to fainter magnitudes, have a higher source density. For the wide fields, the chance of having a neighbour purely at random within $0.5''$ is about 1%. The overlap zones between the wide pointings are typically a few arcminutes wide; having 1% of the sources in these non-negligible zones be missed is not acceptable.

Therefore, a hybrid method was adopted. The Wide fields were divided into grids as above but the boundaries were expanded by $\theta_{overlap}$ arcseconds for each pointing so that they overlapped only slightly. The overlap zone was now only $2\theta_{overlap}$ arcseconds wide. Setting $\theta_{overlap} = 10''$ was large enough to accommodate the positional uncertainty of even fairly large, fuzzy objects, but small enough that missing 1% of the objects in these zones is acceptable. Sources in each pointing catalog outside the boundaries were trimmed. The trimmed catalogs were combined. Objects from different pointing catalogs lying with $\theta_{match} = 0.5''$ of each other were deemed to be the same object; the second entry was removed.

There are two parameters in this method: $\theta_{overlap}$ and θ_{match} . Changing either parameter significantly (doubling or halving it) had only a very small effect on the final merged catalogs: the total number of sources would change by a few hundred in a catalog of 30 million sources.

Boundaries were also applied at the edges of the fields. These boundaries lie at the point where the effective exposure time of the images (as indicated by weight map) drops to half of the nominal value.

8. QUALITY CONTROL

8.1. Astrometry

8.1.1. Internal Astrometric Consistency

The internal accuracy was checked by running SExtractor on each stacked image in every band and obtaining catalogs of object positions. The positional catalogs for each band were

matched to each other and common objects identified. If the astrometry was perfect, then the position of an object in each band would be identical. In practice, there are astrometric residuals. Examining these residuals gives an idea of the astrometric uncertainties.

Figure 13 shows checks on the internal astrometry between the g' and r' band images for the D2 field. The top left quarter shows the direction and size (greatly enlarged) of the astrometric residuals as line segments. This plot is an important diagnostic of astrometry because, while the residuals are typically quite small, there are outliers in any distribution. As long as these outliers are relatively isolated from each other and pointing in random directions all is well. Conversely, if there are a number large of residuals in close proximity to each other, all pointing the same direction, this indicates a systematic misalignment between the two images in question. The figure shows no such misalignments. Similar plots were made for every possible pair of images in the CFHTLS. No misalignments or other problems were found, indicating there are no systematic astrometric errors.

The two right panels show the residuals in RA and Dec separately, which are about 0.02 arcseconds (68%-tile). The bottom left quarter shows the astrometric residuals in RA and Dec. The red histograms show the relative distribution of the residuals in both directions. The 68%-tile of the residuals is 0.03 arcseconds radially, about $\sqrt{2}$ larger than the residuals in any one direction.

In general, the internal astrometric uncertainties are slightly larger than the example shown in Figure 13. Similar plots were made for every possible pair of images in the CFHTLS. The typical internal astrometric residuals are 0.04" in any one direction. However, no misalignments or other problems were found, indicating there are no systematic astrometric errors.

8.1.2. *External Astrometric Accuracy*

Accurate astrometry relative to external systems is relevant for follow-up observations with other telescopes. External accuracy was checked by matching each catalog for each field and filter back to the astrometric reference catalog. Again, the scatter in the astrometric residuals is a measure of the uncertainty and the presence of any localized large residuals indicates a systematic shift. Figure 14 shows an example of the astrometric residuals of one of the pointings with respect to the SDSS. The panels have the same meanings as in Figure 13. The external residuals are larger than the internal residuals. Similar plots were generated for all pointings and bands. On average, the astrometric residuals are 0.07 arcseconds with respect to the SDSS and 0.18 arcseconds with respect to NOMAD. No systematic offsets are

visible, indicating that they are smaller than the random residuals, if indeed they exist.

8.2. Photometry

8.2.1. Internal Consistency

The edges of the Wide pointings overlap. Comparing the photometry of objects in the overlap regions gives a measure of the photometric consistency. Systematic difference in photometry indicate zero-point offsets. Figure 9 shows a histogram of the pointing-to-pointing zero-point differences. In comparing two pointings, the sign of the zero-point difference is irrelevant, so the absolute value of the differences is plotted here. The average offsets are about 0.01 magnitudes, slightly higher for the u^* and z' bands.

8.2.2. External Accuracy

At least some of the pointings of each of the Wide fields as well as the D2 and D3 fields lie within the SDSS. This makes it possible to directly compare the magnitudes in those fields to an external reference. Figure 16 shows a typical comparison between the SDSS (transformed to the MegaCam system as described by Equation 3) and the CFHTLS for the 5 bands. The agreement is very good. At bright magnitudes, for g, r and i bands, there are deviations caused by stars saturating in the MegaCam images. There is no evidence for systematic shifts greater than 0.01 magnitudes. There is also relatively little scatter (at least at moderate magnitudes), which argues that the color terms in the SDSS-MegaCam transformation are fairly accurate. The u^* -band shows greater scatter than the other bands; this is caused by the larger and more uncertain color terms in the transformation between the SDSS and MegaCam photometric systems.

Similar comparisons have been done for every pointing overlapping the SDSS. Figure 17 summarizes the results. The offsets are typically slightly larger than the internal photometric residuals shown above, ranging from 0.010 magnitudes in i' to 0.018 for the u^* -band.

8.2.3. Magnitude limits

The limiting magnitudes of the images were determined by adding fake stars and galaxies to the images and then trying to recover them using the same parameters used to generate the real image catalogs.

The fake galaxies used were taken from the images themselves, rather than adding completely artificial galaxies. A set of 40 bright, isolated galaxies were selected out of the field and assembled into a master list. Postage stamps of these galaxies were cut out of the field. The galaxies were faded in both surface brightness and magnitude through a combination of scaling the pixel values and resampling the images.

To test the recovery rate at a given magnitude and surface brightness, galaxy postage stamps were selected from the master list, faded as described above to the magnitude and surface brightness in question and then added to the image at random locations. SExtractor was then run on new image. The fraction of fake galaxies found gives the recovery rate at that magnitude and surface brightness. An illustration of adding the galaxies is shown in Figure 11 of Gwyn (2008).

To test the false-positive rate, the original image was multiplied by -1; the noise peaks became noise troughs and vice-versa. SExtractor was run, using the same detection criteria. Since there are no real negative galaxies, all the objects thus detected are spurious.

The magnitude/surface brightness plot in Figure 18 shows the results of such tests. The black points are real objects. The bottom edge of the black points is the locus of point-like objects. The green points show the false-positive detections, located at faint magnitudes and surface brightnesses. The red numbers show the percent of artificial galaxies that were recovered at a given magnitude/surface brightness. Superimposed on the numbers are two contour lines in blue, at 50% and 70% completeness.

Deriving a single limiting magnitude from such a plot is slightly difficult. The cleaner cut in the false positives seems to be in surface brightness. Extended objects become harder to detect at brighter magnitudes whereas stellar objects are detectable a magnitude or so fainter.

Point source limiting magnitudes were also calculated. Point sources were added to the images in a similar manner to the above, but only scaled with magnitude. For the Deep fields in particular, the images were effectively crowded. An artificial source added to the image stood a significant chance of ending up close enough to a real source that it would not be detected. To compensate for this, sources were added to two images. The first was just the original image. The second was the original image with all the real sources removed and their pixels replaced with values matching the background noise characteristics; *i.e.*, a blank image. The differences between the two completeness limits is shown in Figure 19. This figure shows the completeness limits for a Wide pointing. The blue line shows the fraction of artificial point sources that can be recovered from the blank image. The red line shows the same for the original image. It is consistently a few 10^{ths} of a magnitude less deep. The black

points show the number counts of real sources. The green points show the number counts for false positive detections. The 50% completeness limit for this image is 25.7 magnitudes. The 50% completeness limits are the values quoted as limiting magnitudes in Tables 1, 2 and 3.

9. DISTRIBUTION

The MegaPipe processed images are available via webpages at the Canadian Astronomy Data Centre³. There are a number of different ways to access the data.

The simplest are webpages which give links to each of the data products. These pages (one each for the Deep “full version”, Deep “best seeing version” and Wide) also allow users to select multiple images and catalogs for parallel download with the CADC’s Download-Manager.

There is also a graphical search tool based on Google Maps which allows users to pan and zoom around the fields, and select images for download. The images are previewed in this tool as RGB color images, constructed using the i' , r' and g' -band images. This tool allows users to select and download image cutouts.

The CFHTLS Deep fields are located at points on the sky which have considerable coverage at other wavelengths, as discussed in Section 2. A set of Google Sky tools, one per Deep fields are provided which allow users to display color previews at these other wavelengths.

The images are large: 1.7 gigabytes or so in size. Many users require only a fraction of the image. Therefore a cutout service is also provided, which can be accessed either via the graphical search tool or by a separate search page. The search page allows users to enter coordinates and retrieve subsections of the images centered on those coordinates. Users can enter a single coordinate or multiple coordinates. The tool also allows users to search by object name. The names are resolved to coordinates using either SIMBAD (Wenger et al. 2007) or NED (Helou et al. 1995) and then the images are searched as before.

The merged catalogs described in section 7.3 can be downloaded directly. They can also be queried using a system similar to the SDSS CasJobs (OMullane et al. 2005). This service allows users to construct arbitrary queries in SQL and retrieve a variety of parameters or combination of parameters.

³<http://www.cadc-ccda.hia-iha.nrc-cnrc.gc.ca/community/CFHTLS-SG/docs/cfhtls.html>

This research used the facilities of the Canadian Astronomy Data Centre operated by the National Research Council of Canada with the support of the Canadian Space Agency.

Based on observations obtained with MegaPrime/MegaCam, a joint project of CFHT and CEA/DAPNIA, at the Canada-France-Hawaii Telescope (CFHT) which is operated by the National Research Council (NRC) of Canada, the Institut National des Sciences de l’Univers of the Centre National de la Recherche Scientifique of France, and the University of Hawaii.

This research has made use of the NASA/IPAC Extragalactic Database (NED) which is operated by the Jet Propulsion Laboratory, California Institute of Technology, under contract with the National Aeronautics and Space Administration.

Funding for the SDSS and SDSS-II has been provided by the Alfred P. Sloan Foundation, the Participating Institutions, the National Science Foundation, the U.S. Department of Energy, the National Aeronautics and Space Administration, the Japanese Monbukagakusho, the Max Planck Society, and the Higher Education Funding Council for England. The SDSS Web Site is <http://www.sdss.org/>.

The SDSS is managed by the Astrophysical Research Consortium for the Participating Institutions. The Participating Institutions are the American Museum of Natural History, Astrophysical Institute Potsdam, University of Basel, University of Cambridge, Case Western Reserve University, University of Chicago, Drexel University, Fermilab, the Institute for Advanced Study, the Japan Participation Group, Johns Hopkins University, the Joint Institute for Nuclear Astrophysics, the Kavli Institute for Particle Astrophysics and Cosmology, the Korean Scientist Group, the Chinese Academy of Sciences (LAMOST), Los Alamos National Laboratory, the Max-Planck-Institute for Astronomy (MPIA), the Max-Planck-Institute for Astrophysics (MPA), New Mexico State University, Ohio State University, University of Pittsburgh, University of Portsmouth, Princeton University, the United States Naval Observatory, and the University of Washington.

Facilities: CFHT.

REFERENCES

- Abazajian, K. N., Adelman-McCarthy, J. K., Agüeros, M. A., Allam, S. S., Allende Prieto, C., An, D., Anderson, K. S. J., Anderson, S. F., Annis, J., Bahcall, N. A., & et al. 2009, *ApJS*, 182, 543
- Astier, P., Guy, J., Regnault, N., Pain, R., Aubourg, E., Balam, D., Basa, S., Carlberg,

- R. G., Fabbro, S., Fouchez, D., Hook, I. M., Howell, D. A., Lafoux, H., Neill, J. D., Palanque-Delabrouille, N., Perrett, K., Pritchett, C. J., Rich, J., Sullivan, M., Taillet, R., Aldering, G., Antilogus, P., Arsenijevic, V., Balland, C., Baumont, S., Bronder, J., Courtois, H., Ellis, R. S., Filiol, M., Gonçalves, A. C., Goobar, A., Guide, D., Hardin, D., Lusset, V., Lidman, C., McMahon, R., Mouchet, M., Mourao, A., Perlmutter, S., Riposte, P., Tao, C., & Walton, N. 2006, *A&A*, 447, 31
- Bertin, E. 2004, http://terapix.iap.fr/rubrique.php?id__rubrique=49
- Bertin, E. & Arnouts, S. 1996, *A&AS*, 117, 393
- Bondi, M., Ciliegi, P., Zamorani, G., Gregorini, L., Vettolani, G., Parma, P., de Ruiter, H., Le Fevre, O., Arnaboldi, M., Guzzo, L., Maccagni, D., Scaramella, R., Adami, C., Bardelli, S., Bolzonella, M., Bottini, D., Cappi, A., Foucaud, S., Franzetti, P., Garilli, B., Gwyn, S., Ilbert, O., Iovino, A., Le Brun, V., Marano, B., Marinoni, C., McCracken, H. J., Meneux, B., Pollo, A., Pozzetti, L., Radovich, M., Ripepi, V., Rizzo, D., Scodreggio, M., Tresse, L., Zanichelli, A., & Zucca, E. 2003, *A&A*, 403, 857
- Bundy, K., Ellis, R. S., Conselice, C. J., Taylor, J. E., Cooper, M. C., Willmer, C. N. A., Weiner, B. J., Coil, A. L., Noeske, K. G., & Eisenhardt, P. R. M. 2006, *ApJ*, 651, 120
- Calabretta, M. R., Valdes, F. G., Greisen, E. W., & Allen, S. L. 2004
- Capak, P., Aussel, H., Ajiki, M., McCracken, H. J., Mobasher, B., Scoville, N., Shopbell, P., Taniguchi, Y., Thompson, D., Tribiano, S., Sasaki, S., Blain, A. W., Brusa, M., Carilli, C., Comastri, A., Carollo, C. M., Cassata, P., Colbert, J., Ellis, R. S., Elvis, M., Giavalisco, M., Green, W., Guzzo, L., Hasinger, G., Ilbert, O., Impey, C., Jahnke, K., Kartaltepe, J., Kneib, J., Koda, J., Koekemoer, A., Komiyama, Y., Leauthaud, A., Le Fevre, O., Lilly, S., Liu, C., Massey, R., Miyazaki, S., Murayama, T., Nagao, T., Peacock, J. A., Pickles, A., Porciani, C., Renzini, A., Rhodes, J., Rich, M., Salvato, M., Sanders, D. B., Scarlata, C., Schiminovich, D., Schinnerer, E., Scodreggio, M., Sheth, K., Shioya, Y., Tasca, L. A. M., Taylor, J. E., Yan, L., & Zamorani, G. 2007, *ApJS*, 172, 99
- Carlberg, R. G., Sullivan, M., & Le Borgne, D. 2009, *ApJ*, 694, 1131
- Chiappetti, L., Tajer, M., Trinchieri, G., Maccagni, D., Maraschi, L., Paiono, L., Pierre, M., Surdej, J., Garcet, O., Gosset, E., Le Fèvre, O., Bertin, E., McCracken, H. J., Mellier, Y., Foucaud, S., Radovich, M., Ripepi, V., & Arnaboldi, M. 2005, *A&A*, 439, 413
- Chiu, L. 1976, *PASP*, 88, 803

- Cuillandre, J., Mellier, Y., Dupin, J., Tilloles, P., Murowinski, R., Crampton, D., Wooff, R., & Luppino, G. A. 1996, *PASP*, 108, 1120
- Cuillandre, J.-C., Magnier, E. A., Isani, S., Sabin, D., Knight, W., Kras, S., & Lai, K. 2002, in Presented at the Society of Photo-Optical Instrumentation Engineers (SPIE) Conference, Vol. 4844, Observatory Operations to Optimize Scientific Return III. Edited by Quinn, Peter J. Proceedings of the SPIE, Volume 4844, pp. 501-507 (2002)., ed. P. J. Quinn, 501–507
- Davis, M., Guhathakurta, P., Konidaris, N. P., Newman, J. A., Ashby, M. L. N., Biggs, A. D., Barmby, P., Bundy, K., Chapman, S. C., Coil, A. L., Conselice, C. J., Cooper, M. C., Croton, D. J., Eisenhardt, P. R. M., Ellis, R. S., Faber, S. M., Fang, T., Fazio, G. G., Georgakakis, A., Gerke, B. F., Goss, W. M., Gwyn, S., Harker, J., Hopkins, A. M., Huang, J., Ivison, R. J., Kassin, S. A., Kirby, E. N., Koekemoer, A. M., Koo, D. C., Laird, E. S., Le Floch, E., Lin, L., Lotz, J. M., Marshall, P. J., Martin, D. C., Metevier, A. J., Moustakas, L. A., Nandra, K., Noeske, K. G., Papovich, C., Phillips, A. C., Rich, R. M., Rieke, G. H., Rigopoulou, D., Salim, S., Schiminovich, D., Simard, L., Smail, I., Small, T. A., Weiner, B. J., Willmer, C. N. A., Willner, S. P., Wilson, G., Wright, E. L., & Yan, R. 2007, *ApJ*, 660, L1
- Erben, T., Hildebrandt, H., Lerchster, M., Hudelot, P., Benjamin, J., van Waerbeke, L., Schrabback, T., Brimiouille, F., Cordes, O., Dietrich, J. P., Holhjem, K., Schirmer, M., & Schneider, P. 2009, *A&A*, 493, 1197
- Goranova, Y., Hudelot, P., Magnar, F., McCracken, H., Mellier, Y., Monnerville, M., Schultheis, M., Sémah, G., Cuillandre, J.-C., & Aussel, H. 2009, <http://terapix.iap.fr/cplt/T0006-doc.pdf>
- Gwyn, S. D. J. 2008, *PASP*, 120, 212
- Hasinger, G., Cappelluti, N., Brunner, H., Brusa, M., Comastri, A., Elvis, M., Finoguenov, A., Fiore, F., Franceschini, A., Gilli, R., Griffiths, R. E., Lehmann, I., Mainieri, V., Matt, G., Matute, I., Miyaji, T., Molendi, S., Paltani, S., Sanders, D. B., Scoville, N., Tresse, L., Urry, C. M., Vettolani, P., & Zamorani, G. 2007, *ApJS*, 172, 29
- Helou, G., Madore, B. F., Schmitz, M., Wu, X., Corwin, Jr., H. G., Lague, C., Bennett, J., & Sun, H. 1995, in *Astrophysics and Space Science Library*, Vol. 203, Information & On-Line Data in Astronomy, ed. D. Egret & M. A. Albrecht, 95–113
- Iovino, A., McCracken, H. J., Garilli, B., Foucaud, S., Le Fèvre, O., Maccagni, D., Saracco, P., Bardelli, S., Busarello, G., Scodreggio, M., Zanichelli, A., Paioro, L., Bottini, D., Le

- Brun, V., Picat, J. P., Scaramella, R., Tresse, L., Vettolani, G., Adami, C., Arnaboldi, M., Arnouts, S., Bolzonella, M., Cappi, A., Charlot, S., Ciliegi, P., Contini, T., Franzetti, P., Gavignaud, I., Guzzo, L., Ilbert, O., Marano, B., Marinoni, C., Mazure, A., Meneux, B., Merighi, R., Paltani, S., Pellò, R., Pollo, A., Pozzetti, L., Radovich, M., Zamorani, G., Zucca, E., Bertin, E., Bondi, M., Bongiorno, A., Cucciati, O., Gregorini, L., Mathez, G., Mellier, Y., Merluzzi, P., Ripepi, V., & Rizzo, D. 2005, *A&A*, 442, 423
- Ivezić, Ž., Lupton, R. H., Schlegel, D., Boroski, B., Adelman-McCarthy, J., Yanny, B., Kent, S., Stoughton, C., Finkbeiner, D., Padmanabhan, N., Rockosi, C. M., Gunn, J. E., Knapp, G. R., Strauss, M. A., Richards, G. T., Eisenstein, D., Nicinski, T., Kleinman, S. J., Krzesinski, J., Newman, P. R., Snedden, S., Thakar, A. R., Szalay, A., Munn, J. A., Smith, J. A., Tucker, D., & Lee, B. C. 2004, *Astronomische Nachrichten*, 325, 583
- Kavelaars, J. J., Jones, R. L., Gladman, B. J., Petit, J., Parker, J. W., Van Laerhoven, C., Nicholson, P., Rousselot, P., Scholl, H., Mousis, O., Marsden, B., Benavidez, P., Bieryla, A., Campo Bagatin, A., Doressoundiram, A., Margot, J. L., Murray, I., & Veillet, C. 2009, *AJ*, 137, 4917
- Laird, E. S., Nandra, K., Georgakakis, A., Aird, J. A., Barmby, P., Conselice, C. J., Coil, A. L., Davis, M., Faber, S. M., Fazio, G. G., Guhathakurta, P., Koo, D. C., Sarajedini, V., & Willmer, C. N. A. 2009, *ApJS*, 180, 102
- Lasker, B. M., Lattanzi, M. G., McLean, B. J., Bucciarelli, B., Drimmel, R., Garcia, J., Greene, G., Guglielmetti, F., Hanley, C., Hawkins, G., Laidler, V. G., Loomis, C., Meakes, M., Mignani, R., Morbidelli, R., Morrison, J., Pannunzio, R., Rosenberg, A., Sarasso, M., Smart, R. L., Spagna, A., Sturch, C. R., Volpicelli, A., White, R. L., Wolfe, D., & Zacchei, A. 2008, *AJ*, 136, 735
- Lawrence, A., Warren, S. J., Almaini, O., Edge, A. C., Hambly, N. C., Jameson, R. F., Lucas, P., Casali, M., Adamson, A., Dye, S., Emerson, J. P., Foucaud, S., Hewett, P., Hirst, P., Hodgkin, S. T., Irwin, M. J., Lodieu, N., McMahon, R. G., Simpson, C., Smail, I., Mortlock, D., & Folger, M. 2007, *MNRAS*, 379, 1599
- Le Fèvre, O., Vettolani, G., Garilli, B., Tresse, L., Bottini, D., Le Brun, V., Maccagni, D., Picat, J. P., Scaramella, R., Scodreggio, M., Zanichelli, A., Adami, C., Arnaboldi, M., Arnouts, S., Bardelli, S., Bolzonella, M., Cappi, A., Charlot, S., Ciliegi, P., Contini, T., Foucaud, S., Franzetti, P., Gavignaud, I., Guzzo, L., Ilbert, O., Iovino, A., McCracken, H. J., Marano, B., Marinoni, C., Mathez, G., Mazure, A., Meneux,

- B., Merighi, R., Paltani, S., Pellò, R., Pollo, A., Pozzetti, L., Radovich, M., Zamorani, G., Zucca, E., Bondi, M., Bongiorno, A., Busarello, G., Lamareille, F., Mellier, Y., Merluzzi, P., Ripepi, V., & Rizzo, D. 2005, *A&A*, 439, 845
- Lilly, S. J., Le Fèvre, O., Crampton, D., Hammer, F., & Tresse, L. 1995, *Astrophys. J.*, 455, 50
- Lilly, S. J., Le Fèvre, O., Renzini, A., Zamorani, G., Scodreggio, M., Contini, T., Carollo, C. M., Hasinger, G., Kneib, J., Iovino, A., Le Brun, V., Maier, C., Mainieri, V., Mignoli, M., Silverman, J., Tasca, L. A. M., Bolzonella, M., Bongiorno, A., Bottini, D., Capak, P., Caputi, K., Cimatti, A., Cucciati, O., Daddi, E., Feldmann, R., Franzetti, P., Garilli, B., Guzzo, L., Ilbert, O., Kampczyk, P., Kovac, K., Lamareille, F., Leauthaud, A., Borgne, J., McCracken, H. J., Marinoni, C., Pello, R., Ricciardelli, E., Scarlata, C., Vergani, D., Sanders, D. B., Schinnerer, E., Scoville, N., Taniguchi, Y., Arnouts, S., Aussel, H., Bardelli, S., Brusa, M., Cappi, A., Ciliegi, P., Finoguenov, A., Foucaud, S., Franceschini, R., Halliday, C., Impey, C., Knobel, C., Koekemoer, A., Kurk, J., Maccagni, D., Maddox, S., Marano, B., Marconi, G., Meneux, B., Mobasher, B., Moreau, C., Peacock, J. A., Porciani, C., Pozzetti, L., Scaramella, R., Schiminovich, D., Shopbell, P., Smail, I., Thompson, D., Tresse, L., Vettolani, G., Zanichelli, A., & Zucca, E. 2007, *ApJS*, 172, 70
- Magnier, E. A. & Cuillandre, J.-C. 2004, *PASP*, 116, 449
- McCracken, H. J., Radovich, M., Bertin, E., Mellier, Y., Dantel-Fort, M., Le Fèvre, O., Cuillandre, J. C., Gwyn, S., Foucaud, S., & Zamorani, G. 2003, *A&A*, 410, 17
- Oke, J. B. 1974, *ApJS*, 27, 21
- OMullane, W., Li, N., Nieto-Santisteban, M., Szalay, A., Thakar, A., & Gray, J. 2005, *ArXiv Computer Science e-prints*
- Regnault, N., Conley, A., Guy, J., Sullivan, M., Cuillandre, J., Astier, P., Balland, C., Basa, S., Carlberg, R. G., Fouchez, D., Hardin, D., Hook, I. M., Howell, D. A., Pain, R., Perrett, K., & Pritchett, C. J. 2009, *A&A*, 506, 999
- Sanders, D. B., Salvato, M., Aussel, H., Ilbert, O., Scoville, N., Surace, J. A., Frayer, D. T., Sheth, K., Helou, G., Brooke, T., Bhattacharya, B., Yan, L., Kartaltepe, J. S., Barnes, J. E., Blain, A. W., Calzetti, D., Capak, P., Carilli, C., Carollo, C. M., Comastri, A., Daddi, E., Ellis, R. S., Elvis, M., Fall, S. M., Franceschini, A., Giavalisco, M., Hasinger, G., Impey, C., Koekemoer, A., Le Fèvre, O., Lilly, S., Liu, M. C., McCracken, H. J., Mobasher, B., Renzini, A., Rich, M., Schinnerer, E., Shopbell, P. L., Taniguchi, Y., Thompson, D. J., Urry, C. M., & Williams, J. P. 2007, *ApJS*, 172, 86

- Schinnerer, E., Smolčić, V., Carilli, C. L., Bondi, M., Ciliegi, P., Jahnke, K., Scoville, N. Z., Aussel, H., Bertoldi, F., Blain, A. W., Impey, C. D., Koekemoer, A. M., Le Fevre, O., & Urry, C. M. 2007, *ApJS*, 172, 46
- Scoville, N., Aussel, H., Brusa, M., Capak, P., Carollo, C. M., Elvis, M., Giavalisco, M., Guzzo, L., Hasinger, G., Impey, C., Kneib, J., LeFevre, O., Lilly, S. J., Mobasher, B., Renzini, A., Rich, R. M., Sanders, D. B., Schinnerer, E., Schminovich, D., Shopbell, P., Taniguchi, Y., & Tyson, N. D. 2007, *ApJS*, 172, 1
- Setson, P. B. 1989, lectures presented at the Universidade de Sao Paulo, http://nedwww.ipac.caltech.edu/level5/Stetson/Stetson_contents.html
- Smith, J. A., Tucker, D. L., Kent, S., Richmond, M. W., Fukugita, M., Ichikawa, T., Ichikawa, S.-i., Jorgensen, A. M., Uomoto, A., Gunn, J. E., Hamabe, M., Watanabe, M., Tolea, A., Henden, A., Annis, J., Pier, J. R., McKay, T. A., Brinkmann, J., Chen, B., Holtzman, J., Shimasaku, K., & York, D. G. 2002, *AJ*, 123, 2121
- Steidel, C. C., Adelberger, K. L., Shapley, A. E., Pettini, M., Dickinson, M., & Giavalisco, M. 2003, *ApJ*, 592, 728
- Walcher, C. J., Lamareille, F., Vergani, D., Arnouts, S., Buat, V., Charlot, S., Tresse, L., Le Fèvre, O., Bolzonella, M., Brinchmann, J., Pozzetti, L., Zamorani, G., Bottini, D., Garilli, B., Le Brun, V., Maccagni, D., Milliard, B., Scaramella, R., Scodreggio, M., Vettolani, G., Zanichelli, A., Adami, C., Bardelli, S., Cappi, A., Ciliegi, P., Contini, T., Franzetti, P., Foucaud, S., Gavignaud, I., Guzzo, L., Ilbert, O., Iovino, A., McCracken, H. J., Marano, B., Marinoni, C., Mazure, A., Meneux, B., Merighi, R., Paltani, S., Pellò, R., Pollo, A., Radovich, M., Zucca, E., Lonsdale, C., & Martin, C. 2008, *A&A*, 491, 713
- Wenger, M., Oberto, A., Bonnarel, F., Brouty, M., Bruneau, C., Brunet, C., Cambresy, L., Dubois, P., Eisele, A., Fernique, P., Genova, F., Laloë, S., Lesteven, S., Loup, C., Oksenbein, F., Vannier, P. J., Vollmer, B., Vonflie, P., Wagner, M. J., Woelfel, F., Borde, S., Beyneix, A., Chassagnard, G., Jasniewicz, G., & Davoust, E. 2007, in *Astronomical Society of the Pacific Conference Series*, Vol. 377, Library and Information Services in Astronomy V, ed. S. Ricketts, C. Birdie, & E. Isaksson, 197–+
- Zacharias, N., Monet, D. G., Levine, S. E., Urban, S. E., Gaume, R., & Wycoff, G. L. 2004, in *Bulletin of the American Astronomical Society*, Vol. 36, *Bulletin of the American Astronomical Society*, 1418–+

Zamojski, M. A., Schiminovich, D., Rich, R. M., Mobasher, B., Koekemoer, A. M., Capak, P., Taniguchi, Y., Sasaki, S. S., McCracken, H. J., Mellier, Y., Bertin, E., Aussel, H., Sanders, D. B., Le Fèvre, O., Ilbert, O., Salvato, M., Thompson, D. J., Kartaltepe, J. S., Scoville, N., Barlow, T. A., Forster, K., Friedman, P. G., Martin, D. C., Morrissey, P., Neff, S. G., Seibert, M., Small, T., Wyder, T. K., Bianchi, L., Donas, J., Heckman, T. M., Lee, Y., Madore, B. F., Milliard, B., Szalay, A. S., Welsh, B. Y., & Yi, S. K. 2007, ApJS, 172, 468

This preprint was prepared with the AAS L^AT_EX macros v5.2.

Table 1. Deep full stacks: limiting magnitudes and image qualities

Field	u^*		g'		r'		i'		z'	
	m_{lim}	IQ (")	m_{lim}	IQ (")	m_{lim}	IQ (")	m_{lim}	IQ (")	m_{lim}	IQ (")
D1	27.4	0.94	27.9	0.89	27.6	0.83	27.4	0.78	26.1	0.81
D2	27.5	0.96	27.9	0.92	27.6	0.84	27.3	0.83	26.4	0.83
D3	27.4	0.97	28.0	0.94	27.8	0.83	27.6	0.80	26.4	0.78
D4	27.3	0.96	27.8	0.91	27.7	0.83	27.2	0.80	26.2	0.78

Table 2. Deep good seeing stacks: limiting magnitudes and image qualities

Field	u^*		g'		r'		i'		z'	
	m_{lim}	IQ (")	m_{lim}	IQ (")	m_{lim}	IQ (")	m_{lim}	IQ (")	m_{lim}	IQ (")
D1	27.1	0.80	27.2	0.64	27.3	0.64	27.3	0.64	25.9	0.64
D2	27.4	0.80	27.4	0.65	27.4	0.64	27.1	0.64	26.2	0.64
D3	27.1	0.78	27.5	0.65	27.5	0.64	27.3	0.64	26.1	0.64
D4	26.8	0.78	27.0	0.64	27.0	0.64	26.8	0.64	25.9	0.64

Table 3. Wide stacks: limiting magnitudes and image qualities

Pointing	u^*		g'		r'		i'		z'	
	m_{lim}	IQ (")	m_{lim}	IQ (")	m_{lim}	IQ (")	m_{lim}	IQ (")	m_{lim}	IQ (")
W1+0+0	26.1	0.83	26.4	0.86	26.0	0.75	25.8	0.74	24.0	0.96
W1+0+1	25.7	1.01	26.3	0.91	26.1	0.83	26.0	0.64	24.9	0.78
W1+0+2	25.9	0.97	26.5	0.92	25.8	0.86	26.0	0.57	24.6	0.84
W1+0+3	26.0	0.86	26.3	0.90	25.7	0.92	25.7	0.80	24.5	0.90
W1+0-1	26.0	1.06	26.5	0.89	25.9	0.79	25.9	0.55	24.1	1.01
W1+0-2	25.9	1.11	26.8	0.66	25.8	0.84	25.8	0.69	24.7	0.66
W1+0-3	26.2	1.09	26.5	0.91	25.8	0.86	25.8	0.72	24.5	0.78
W1+0-4	26.1	0.84	26.6	0.95	25.9	0.77	25.6	0.71	25.0	0.56
W1+1+0	26.3	0.85	26.6	0.79	25.9	0.73	25.8	0.57	24.5	0.84
W1+1+1	25.8	0.97	26.7	0.92	25.8	0.84	26.0	0.86	25.1	0.79
W1+1+2	25.7	1.03	26.2	0.86	26.1	0.67	25.5	0.81	24.9	0.69
W1+1+3	26.0	0.88	26.5	0.83	25.9	0.95	25.6	0.80	24.9	0.68
W1+1-1	26.0	0.97	26.6	0.98	26.0	0.74	26.3	0.81	24.2	0.95
W1+1-2	26.0	1.10	26.7	0.76	25.9	0.84	26.0	0.81	24.6	0.78
W1+1-3	26.1	1.05	26.5	0.81	25.8	0.82	25.7	0.70	24.7	0.80
W1+1-4	26.1	0.92	26.6	0.93	26.1	0.76	25.9	0.66	24.9	0.58
W1+2+0	25.7	1.01	26.5	0.86	26.0	0.82	25.4	0.74	24.3	0.87
W1+2+1	25.9	1.06	26.3	1.07	25.7	0.88	25.5	0.88	25.0	0.68
W1+2+2	25.9	0.96	26.3	0.91	25.7	0.89	25.9	0.88	24.7	0.82
W1+2+3	26.3	1.00	26.5	0.83	26.2	0.70	25.6	0.78	25.2	0.60
W1+2-1	26.3	0.96	26.6	0.78	26.0	0.72	25.7	0.77	24.5	1.02
W1+2-2	26.1	1.10	26.5	0.77	25.9	0.73	25.8	0.69	24.2	1.00
W1+2-3	26.3	0.81	26.6	0.73	25.8	0.81	25.5	0.73	24.4	0.92
W1+2-4	26.1	0.89	26.7	0.85	25.8	0.77	25.7	0.75	24.9	0.61
W1+3+0	26.3	0.64	26.3	0.92	25.9	0.83	25.7	0.73	24.6	0.86
W1+3+1	26.1	0.90	26.4	0.99	25.8	0.82	25.8	0.87	24.5	0.82
W1+3+2	26.2	1.10	26.3	0.87	25.9	0.83	25.6	0.70	24.6	0.64
W1+3+3	25.7	1.25	26.3	0.90	25.7	0.82	25.3	0.87	24.7	0.62
W1+3-1	25.9	1.05	26.5	0.80	26.1	0.74	25.8	0.77	24.8	0.74
W1+3-2	26.4	0.85	26.6	0.74	25.8	0.74	25.8	0.72	24.6	0.82
W1+3-3	26.2	0.80	26.7	0.67	25.8	0.87	25.7	0.64	24.5	0.90
W1+3-4	26.0	1.04	26.3	0.90	25.8	0.78	26.1	0.66	24.8	0.63

Table 3—Continued

Pointing	u^*		g'		r'		i'		z'	
	m_{lim}	IQ (")	m_{lim}	IQ (")	m_{lim}	IQ (")	m_{lim}	IQ (")	m_{lim}	IQ (")
W1+4+0	26.4	0.75	26.5	0.91	25.9	0.74	25.3	0.70	24.7	0.75
W1+4+1	26.3	0.84	26.4	0.87	25.7	0.76	25.3	0.84	25.0	0.49
W1+4+2	26.3	0.79	26.7	0.90	25.9	0.67	25.6	0.94	24.8	0.61
W1+4+3	26.0	1.00	26.4	0.89	25.8	0.78	25.2	0.88	24.2	0.86
W1+4-1	25.9	1.17	26.6	0.89	25.9	0.77	26.0	0.61	24.5	0.85
W1+4-2	26.4	0.74	26.6	0.81	25.9	0.73	25.9	0.73	24.4	0.75
W1+4-3	26.0	0.94	26.5	0.85	25.7	0.92	25.8	0.73	24.5	0.79
W1+4-4	26.2	0.91	26.1	1.00	26.1	0.92	26.0	0.83	24.8	0.62
W1-1+0	26.0	0.97	26.5	0.73	26.0	0.74	25.7	0.64	24.3	0.87
W1-1+1	26.1	1.06	26.7	1.02	25.8	0.83	25.9	0.62	24.5	0.79
W1-1+2	25.9	0.96	26.5	0.92	25.9	0.88	25.7	0.64	25.0	0.72
W1-1+3	26.1	0.80	26.4	1.00	25.8	0.89	25.6	0.81	24.9	0.66
W1-1-1	26.7	0.70	26.9	0.59	25.7	0.90	25.9	0.58	24.1	0.91
W1-1-2	26.3	0.83	26.9	0.62	26.0	0.75	25.6	0.86	24.1	1.03
W1-1-3	26.3	0.76	26.2	1.01	25.8	0.77	25.7	0.71	24.5	1.01
W1-1-4	26.4	0.70	26.7	1.05	25.9	0.76	25.5	0.88	24.8	0.68
W1-2+0	26.5	0.82	26.8	0.64	25.8	0.84	26.1	0.52	24.4	0.96
W1-2+1	26.4	0.81	26.8	0.72	25.9	0.75	25.4	0.89	24.9	0.76
W1-2+2	26.4	0.79	26.2	0.92	25.9	0.73	25.2	0.82	24.4	0.88
W1-2+3	26.2	0.83	26.1	0.90	26.0	0.74	25.3	0.76	24.4	0.67
W1-2-1	26.3	0.79	26.9	0.66	25.9	0.86	26.1	0.50	24.5	1.07
W1-2-2	26.3	0.79	26.6	0.70	26.1	0.76	25.9	0.53	24.8	0.62
W1-2-3	26.4	0.72	26.3	0.81	25.8	0.83	25.8	0.65	24.2	1.05
W1-2-4	26.3	0.92	26.5	0.96	26.0	0.75	26.0	0.58	25.2	0.55
W1-3+0	26.0	0.88	26.3	0.98	25.9	0.85	25.6	0.78	24.7	0.65
W1-3+1	26.3	0.90	26.3	0.86	25.9	0.85	25.6	0.79	24.7	0.59
W1-3+2	26.3	0.86	26.1	0.98	25.7	0.89	25.7	0.77	24.8	0.66
W1-3+3	26.1	0.85	26.7	0.75	25.8	0.68	25.7	0.74	24.6	0.67
W1-3-1	25.9	1.01	26.5	0.80	25.9	0.97	25.6	0.82	24.9	0.52
W1-3-2	25.8	1.10	26.6	0.69	25.8	0.83	25.5	0.75	24.7	0.74
W1-3-3	26.0	0.74	26.6	0.70	25.9	0.75	25.8	0.75	24.9	0.73
W1-3-4	26.3	0.97	26.4	0.89	26.1	0.78	25.8	0.65	25.0	0.55

Table 3—Continued

Pointing	u^*		g'		r'		i'		z'	
	m_{lim}	IQ (")	m_{lim}	IQ (")	m_{lim}	IQ (")	m_{lim}	IQ (")	m_{lim}	IQ (")
W1-4+0	25.9	1.05	26.2	0.90	25.8	0.90	26.0	0.61	24.5	0.74
W1-4+1	25.7	1.09	26.2	0.98	25.7	0.88	25.7	0.71	24.7	0.74
W1-4+2	25.8	1.10	26.6	1.05	25.8	0.77	25.6	0.68	24.5	0.88
W1-4+3	26.2	0.85	26.3	0.85	26.0	0.72	25.5	0.74	24.3	0.94
W1-4-1	26.4	0.87	26.4	0.77	25.7	0.94	25.6	0.73	24.0	1.03
W1-4-2	26.5	0.84	26.2	0.93	25.6	1.02	25.7	0.70	24.6	1.06
W1-4-3	26.0	0.88	26.5	0.92	25.5	1.01	25.5	0.69	24.4	0.89
W1-4-4	26.1	0.81	26.5	0.84	25.5	0.90	25.8	0.90	24.6	0.64
W2+0+0	25.9	0.96	26.6	0.90	25.9	0.72	25.7	0.77	24.3	0.91
W2+0+1	26.0	0.94	26.2	0.88	25.7	0.88	25.7	0.61	24.6	0.55
W2+0+2	25.7	1.08	26.4	0.91	26.0	0.63	25.9	0.73	24.4	0.93
W2+0+3	26.1	0.81	26.2	0.74	25.9	0.83	25.6	0.56	24.2	0.84
W2+0-1	25.9	1.20	26.1	0.98	25.7	0.93	25.7	0.66	24.5	1.09
W2+1+0	26.0	0.79	26.6	0.85	25.6	0.92	25.6	0.77	24.6	0.89
W2+1+1	25.9	0.99	26.4	0.81	25.9	0.91	25.7	0.86	24.7	0.85
W2+1+2	25.9	1.25	26.2	0.92	26.0	0.87	25.5	0.83	24.5	0.70
W2+1+3	25.9	1.08	26.2	0.91	26.0	0.81	25.4	0.88	24.5	0.77
W2+1-1	26.3	0.83	26.0	0.92	25.5	1.05	25.5	0.80	24.6	0.74
W2+2+0	25.9	0.97	26.2	0.83	25.7	0.81	25.7	0.78	24.4	1.01
W2+2+1	26.0	1.01	26.3	0.78	25.9	0.79	25.8	0.58	24.7	0.81
W2+2+2	26.1	1.19	26.3	0.80	26.5	0.63	26.0	0.84	24.6	0.79
W2+2+3	26.0	0.88	26.9	0.66	26.0	0.81	25.4	0.86	24.5	0.93
W2+2-1	26.4	0.75	26.3	0.94	25.7	0.78	25.6	0.78	24.6	0.81
W2+3+0	25.9	0.92	26.3	0.85	25.6	0.99	25.9	0.60	24.9	0.82
W2+3+1	26.3	0.88	26.3	0.93	26.0	0.75	25.2	0.89	24.5	0.79
W2+3+2	26.1	1.02	26.3	0.97	25.9	0.80	25.5	0.80	25.0	0.76
W2+3+3	26.4	0.84	26.4	0.99	26.1	0.85	25.5	0.65	24.5	0.90
W2+3-1	26.3	1.01	26.2	0.86	25.7	0.82	25.4	0.83	24.7	0.64
W2-1+0	25.8	1.01	27.0	0.58	25.9	0.73	26.0	0.57	24.6	0.80
W2-1+1	26.0	0.89	26.5	1.02	25.9	0.94	25.9	0.68	24.3	0.89
W2-1+2	25.9	1.16	26.6	0.80	25.7	0.84	25.8	0.55	24.6	0.80
W2-1+3	25.7	1.10	26.7	0.76	26.3	0.67	25.7	0.73	24.5	0.77

Table 3—Continued

Pointing	u^*		g'		r'		i'		z'	
	m_{lim}	IQ (")	m_{lim}	IQ (")	m_{lim}	IQ (")	m_{lim}	IQ (")	m_{lim}	IQ (")
W2-1-1	25.6	0.96	26.5	0.98	25.8	0.84	25.8	0.69	24.6	0.78
W3+0+0	25.6	1.03	26.3	0.96	25.5	0.95	25.3	0.83	24.2	0.81
W3+0+1	25.9	0.99	26.4	0.90	25.6	0.91	25.7	0.72	24.7	0.77
W3+0+2	25.6	1.06	26.4	0.85	25.9	0.79	25.6	0.71	24.4	0.85
W3+0+3	26.0	0.96	26.4	0.84	26.1	0.60	25.5	0.64	24.8	0.92
W3+0-1	25.6	0.99	26.0	1.08	25.8	1.13	25.9	0.72	25.2	0.80
W3+0-2	26.3	0.82	26.4	0.84	25.6	1.00	25.5	0.69	24.6	0.75
W3+0-3	26.1	0.75	26.2	0.91	25.9	0.92	25.1	0.80	24.8	0.86
W3+1+0	26.3	0.82	26.4	0.87	25.8	0.90	25.4	0.75	24.6	0.99
W3+1+1	26.0	0.95	26.5	0.83	25.7	0.89	25.7	0.77	24.7	0.77
W3+1+2	26.5	0.88	26.6	0.72	26.0	0.73	25.9	0.69	24.5	0.78
W3+1+3	26.4	0.84	26.3	0.87	26.1	0.77	25.7	0.70	24.7	0.82
W3+1-1	25.6	1.16	26.4	0.90	25.7	0.92	25.6	0.72	24.6	1.00
W3+1-2	25.8	1.17	26.5	0.83	25.5	0.93	25.4	0.79	24.5	0.84
W3+1-3	25.7	1.16	26.7	1.02	26.0	0.87	25.7	0.72	24.6	0.83
W3+2+0	26.0	0.91	26.7	0.89	25.8	0.85	25.6	0.76	24.5	0.64
W3+2+1	26.3	0.76	26.6	0.97	26.0	0.72	25.7	0.85	24.4	0.83
W3+2+2	26.6	0.65	26.4	0.83	25.8	0.81	25.7	0.60	24.5	0.65
W3+2+3	26.0	1.00	26.5	0.74	26.0	0.66	25.6	0.73	25.0	0.72
W3+2-1	26.2	0.90	26.4	0.94	25.9	1.03	25.7	0.74	24.3	0.74
W3+2-2	26.3	0.84	26.6	0.89	25.5	1.02	25.9	0.64	24.7	0.61
W3+2-3	26.3	0.87	26.6	0.97	25.6	0.99	25.5	0.67	24.7	0.61
W3+3+0	26.0	1.02	26.3	1.02	26.0	0.79	25.8	0.69	24.6	0.82
W3+3+1	26.1	0.91	26.4	1.01	25.9	0.80	25.5	0.90	24.3	0.73
W3+3+2	25.9	0.96	26.3	0.94	26.1	0.71	25.6	0.81	24.2	0.74
W3+3+3	25.9	0.95	26.3	0.72	26.1	0.71	25.5	0.81	25.3	0.68
W3+3-1	26.1	0.90	26.7	0.91	25.9	0.83	25.7	0.94	24.7	0.71
W3+3-2	26.3	1.01	26.6	1.02	25.9	0.85	25.6	0.67	24.8	0.66
W3+3-3	26.3	0.89	26.6	0.95	25.9	0.85	25.6	0.82	24.7	0.72
W3-1+0	26.1	0.71	26.3	1.07	26.0	0.75	25.4	0.60	24.1	0.89
W3-1+1	26.1	0.89	26.5	0.78	25.7	0.89	25.5	0.85	24.4	0.88
W3-1+2	25.7	1.03	26.7	0.77	25.8	0.87	25.6	0.72	24.5	0.78

Table 3—Continued

Pointing	u^*		g'		r'		i'		z'	
	m_{lim}	IQ (")	m_{lim}	IQ (")	m_{lim}	IQ (")	m_{lim}	IQ (")	m_{lim}	IQ (")
W3-1+3	26.1	0.98	26.3	0.89	25.7	0.82	26.1	0.89	24.6	0.68
W3-1-1	25.9	1.03	26.7	0.80	25.6	0.83	25.6	0.60	24.3	0.88
W3-1-2	25.3	0.90	26.3	0.91	26.0	0.75	25.4	0.72	24.6	0.73
W3-1-3	25.7	0.77	26.5	0.88	25.5	0.90	25.7	0.72	24.7	0.66
W3-2+0	26.2	0.72	26.5	0.75	26.2	0.73	25.1	0.82	24.8	0.62
W3-2+1	26.1	0.88	26.6	0.89	25.8	0.91	25.7	0.87	24.7	0.74
W3-2+2	25.9	0.94	26.8	0.68	25.8	0.86	25.6	0.63	24.5	0.88
W3-2+3	26.2	0.89	26.5	0.86	26.1	0.78	26.0	0.90	25.1	0.77
W3-2-1	25.8	0.95	26.1	1.02	25.9	0.70	26.0	0.72	24.8	0.60
W3-2-2	26.1	0.79	26.3	0.94	25.9	0.80	25.6	0.71	24.6	0.71
W3-2-3	25.9	1.22	26.4	0.99	25.8	0.84	25.5	0.76	24.2	0.90
W3-3+0	26.1	0.75	26.5	0.77	26.1	0.67	25.8	0.58	24.7	0.68
W3-3+1	26.3	0.70	26.8	0.78	25.7	0.92	26.1	0.92	24.7	0.69
W3-3+2	25.8	1.08	26.7	0.70	26.1	0.88	25.4	0.72	24.9	0.64
W3-3+3	26.2	1.05	26.5	0.81	26.0	0.75	25.6	0.71	24.9	0.75
W3-3-1	25.6	1.00	26.0	0.88	25.8	0.74	25.6	0.79	24.8	0.63
W3-3-2	26.1	0.67	26.5	0.69	25.6	0.78	25.7	0.58	24.8	0.59
W3-3-3	26.1	0.74	26.3	0.84	25.5	0.96	25.8	0.54	24.8	0.64
W4+0+0	25.7	1.14	26.3	0.85	26.1	0.63	25.6	0.74	25.0	0.74
W4+0+1	25.9	0.99	26.4	0.97	26.1	0.62	25.5	0.70	24.6	0.60
W4+0-1	26.2	0.80	26.7	0.86	26.0	0.75	25.9	0.59	24.7	0.56
W4+0-2	26.3	0.75	26.8	0.79	25.9	0.75	25.9	0.66	24.8	0.70
W4+1+0	25.9	0.91	26.4	0.70	25.8	0.75	25.7	0.56	24.7	0.62
W4+1+1	26.2	0.80	26.8	0.60	25.8	0.77	25.9	0.59	24.7	0.60
W4+1-1	25.9	0.92	26.1	0.90	25.9	0.71	26.0	0.67	24.5	0.71
W4+1-2	25.9	0.91	26.2	0.89	26.0	0.67	25.5	0.80	24.8	0.56
W4+2+0	25.9	0.85	26.3	0.73	26.0	0.69	25.9	0.63	24.1	0.86
W4+2-1	25.5	1.07	26.3	0.83	25.8	0.72	25.6	0.73	24.9	0.79
W4+2-2	25.7	1.15	26.3	0.79	25.8	0.68	26.0	0.76	24.8	0.82
W4-1+0	25.7	0.72	26.5	0.90	26.0	0.70	25.7	0.71	24.4	0.81
W4-1+1	26.1	0.80	26.8	0.86	25.9	0.69	25.9	0.87	24.6	0.74
W4-1+2	26.2	0.83	26.7	0.71	25.8	0.66	25.9	0.58	24.3	1.14

Table 3—Continued

Pointing	u^*		g'		r'		i'		z'	
	m_{lim}	IQ (")	m_{lim}	IQ (")	m_{lim}	IQ (")	m_{lim}	IQ (")	m_{lim}	IQ (")
W4-1+3	26.0	0.97	26.5	0.85	25.7	0.83	26.0	0.55	24.1	0.94
W4-1-1	26.1	0.75	26.9	0.90	25.8	0.78	26.1	0.77	24.8	0.55
W4-1-2	26.5	0.64	26.6	0.87	25.9	0.84	25.6	0.80	24.9	0.55
W4-2+0	25.9	1.01	26.5	0.78	25.8	0.82	25.9	0.80	24.6	0.68
W4-2+1	25.4	1.09	26.0	0.91	26.1	0.66	25.2	0.62	24.4	0.87
W4-2+2	25.9	1.01	26.5	0.80	25.7	0.73	25.6	0.74	24.2	0.83
W4-2+3	26.2	0.85	26.5	0.88	25.6	0.91	25.7	0.78	24.3	0.69
W4-3+0	26.0	0.99	26.7	0.74	25.8	0.76	25.4	0.56	24.5	0.87
W4-3+1	26.1	1.06	26.6	0.78	25.8	0.73	25.6	0.48	24.3	0.87
W4-3+2	26.0	0.89	26.4	0.82	25.7	0.66	25.1	0.74	24.5	0.77
W4-3+3	26.0	0.93	26.6	1.06	25.6	0.83	25.9	0.63	24.5	0.71

Table 4: Sextractor detection parameters

Parameter	Value
DETECT_TYPE	CCD
DETECT_MINAREA	3
DETECT_THRESH	1
ANALYSIS_THRESH	1
THRESH_TYPE	RELATIVE
FILTER	Y
FILTER_NAME	gauss_3.0_7x7.conv
DEBLEND_NTHRESH	32
DEBLEND_MINCONT	0.002
CLEAN	Y
CLEAN_PARAM	1.0

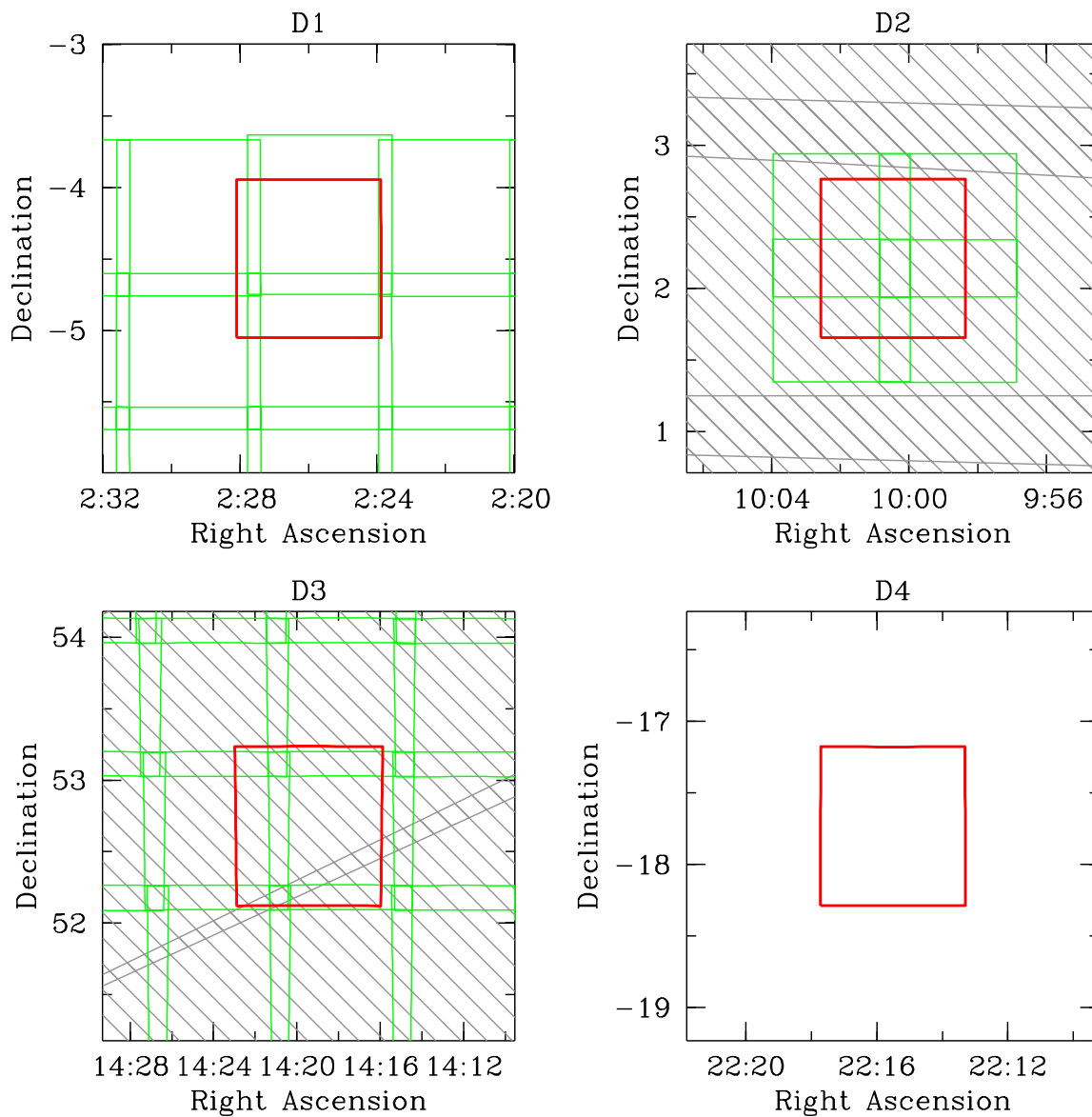


Fig. 1.— Layout of the CFHTLS Deep fields. The red boxes show the four MegaCam pointings. The grey hashed area shows the location of the SDSS. The green boxes in the D1 and D3 panels show the location of the MegaCam W1 and W3 pointings respectively. The green boxes in the D2 panel show the location of the MegaCam COSMOS pointings.

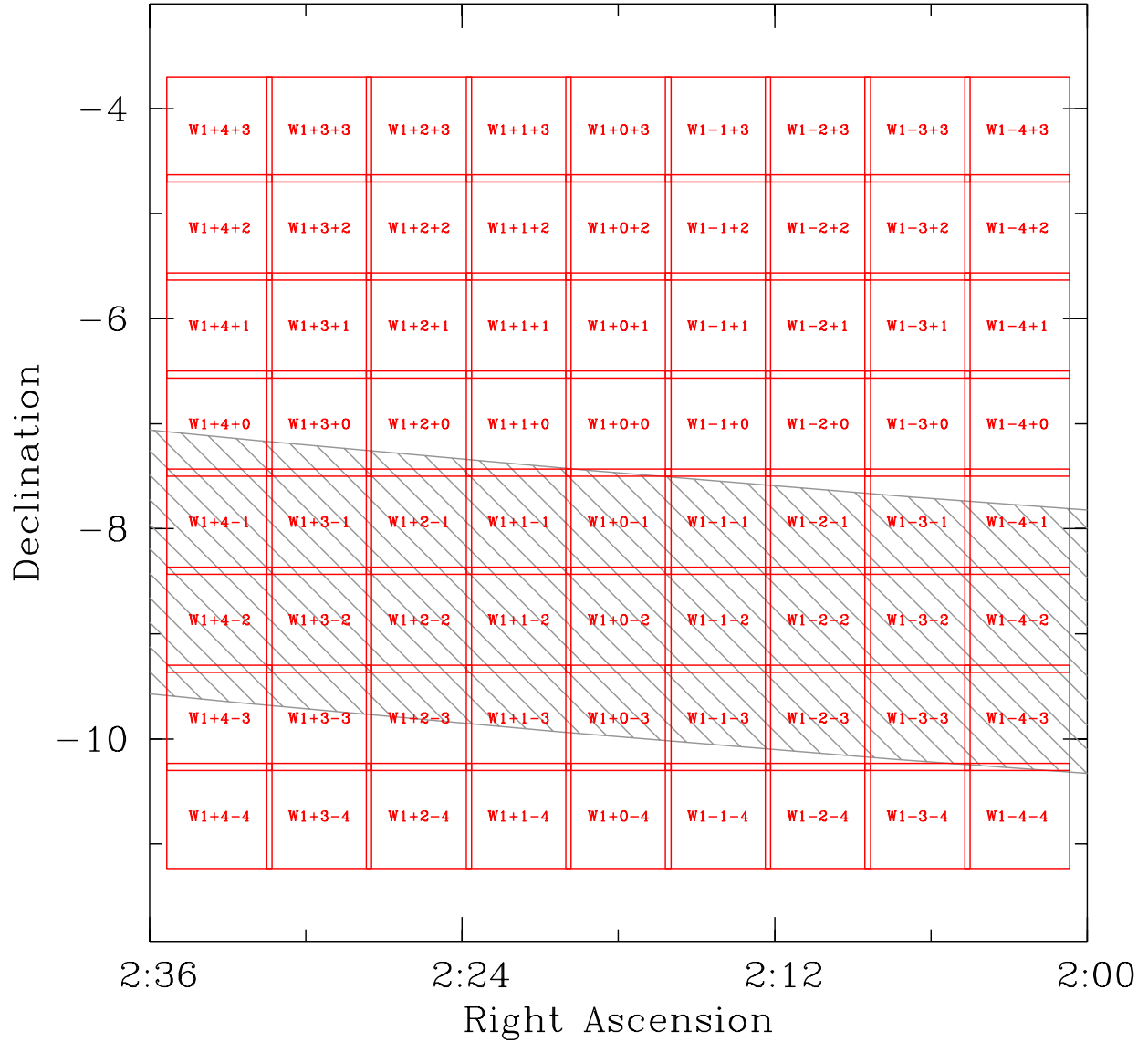


Fig. 2.— Layout of the CFHTLS W1 field. The labelled red boxes show the MegaCam pointings. The grey hashed area shows the location of the SDSS swath, which lies across the middle of the field, overlapping several pointings.

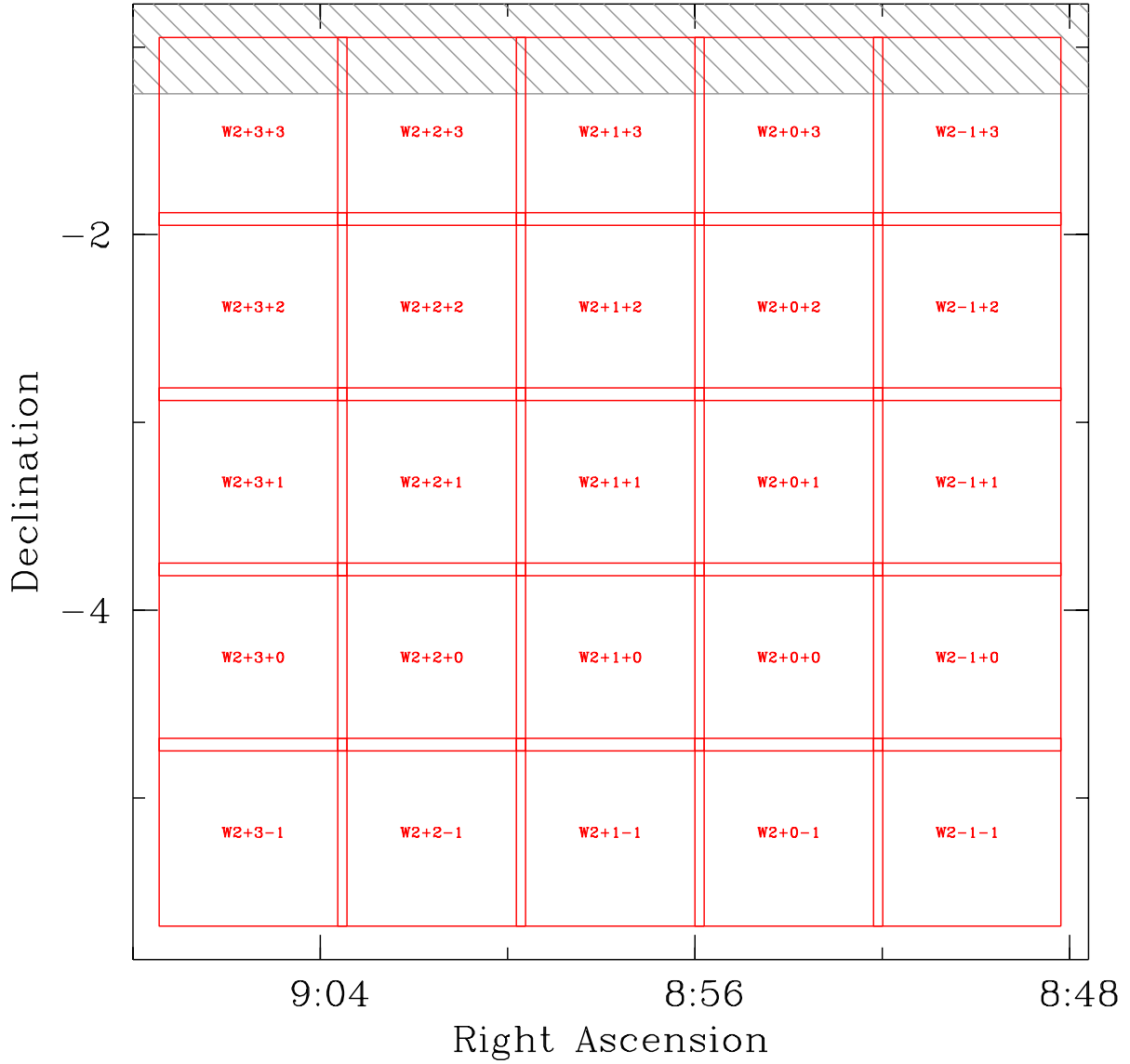


Fig. 3.— Layout of the CFHTLS W2 field. The labelled red boxes show the MegaCam pointings. The grey hashed area shows the locataion of the SDSS swath, which barely overlaps the field.

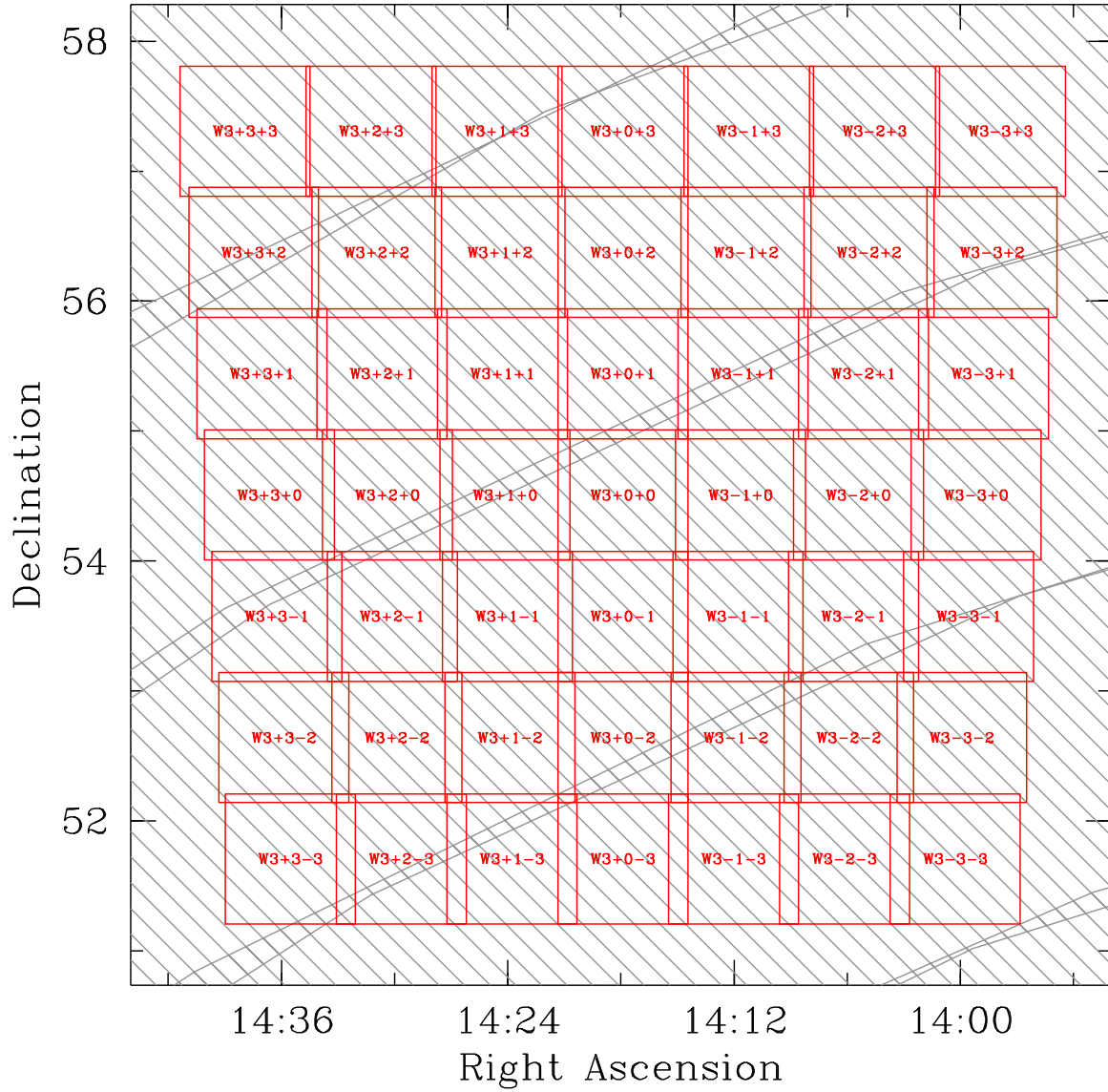


Fig. 4.— Layout of the CFHTLS W3 field. The labelled red boxes show the MegaCam pointings. The W3 field lies completely in the SDSS as shown by the grey hashed area.

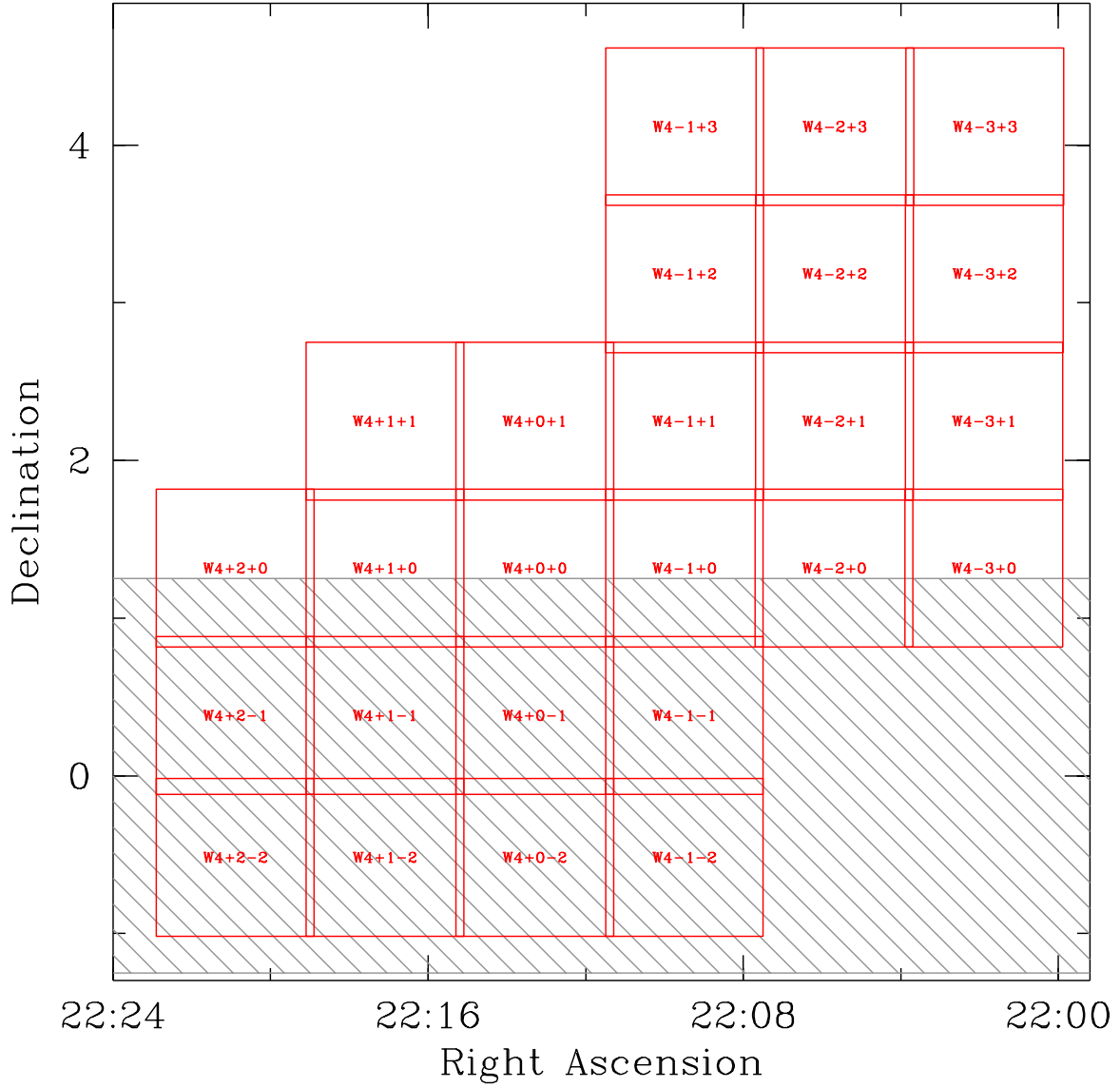


Fig. 5.— Layout of the CFHTLS W4 field. The labelled red boxes show the MegaCam pointings. The grey hashed area shows the location of the SDSS swath which overlaps the field.

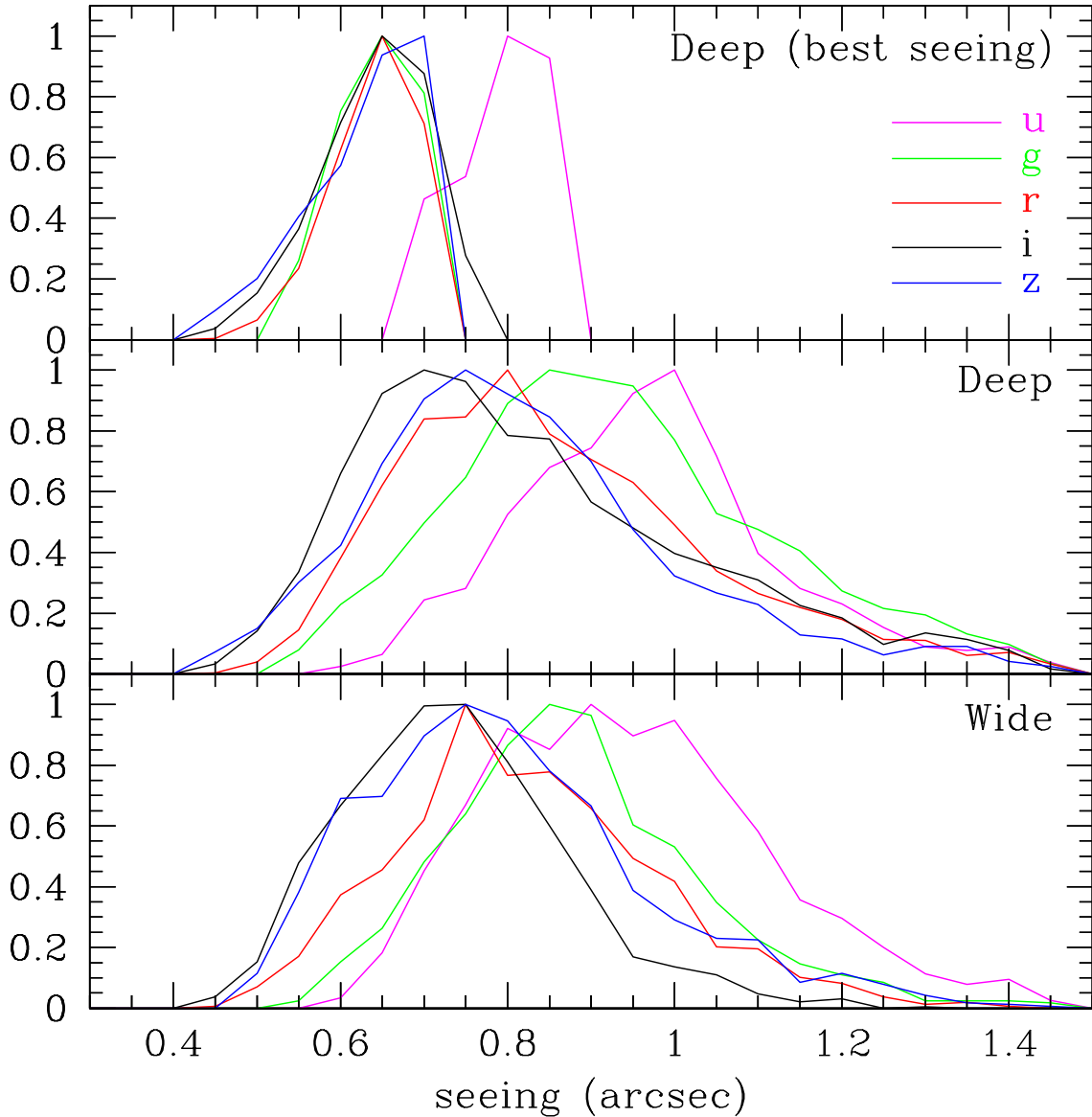


Fig. 6.— Image quality of the CFHTLS input images. The seeing distribution, split by filter, is shown for the different surveys. As discussed in the text, two versions of the Deep survey were generated. The uppermost panel shows the seeing distribution of the input image “good seeing” stacks. The median of the $g'r'i'z'$ image quality is $0.65''$. The median of the u^* image quality is $0.8''$. The distributions are truncated. The middle panel shows the seeing distribution of the input images to the “full” stacks. The bottom panel shows the seeing distribution for the Wide survey.

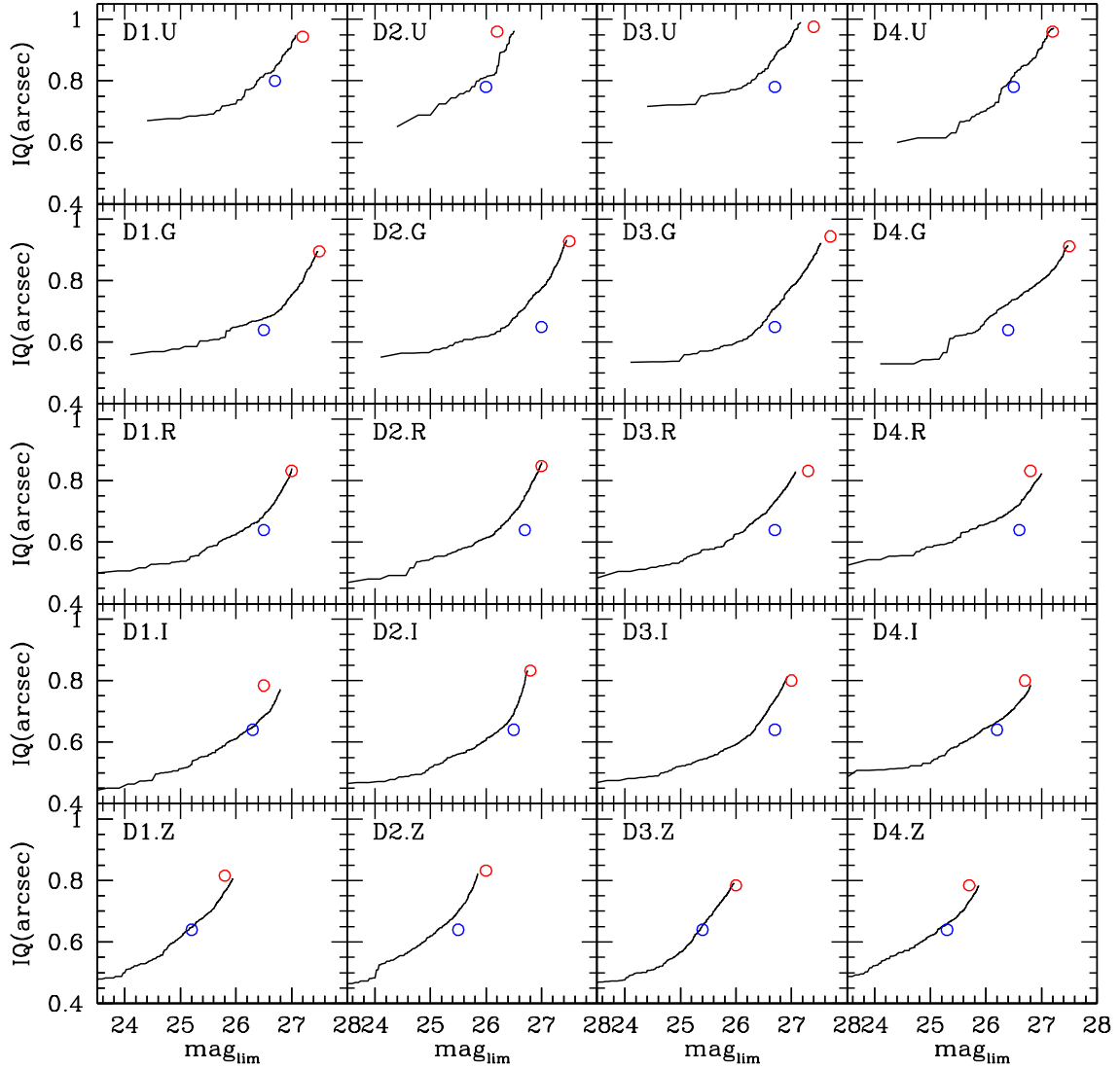


Fig. 7.— Seeing vs limiting magnitude for the CFHTLS Deep fields. If the input images are sorted by image quality, as more images are stacked, the output image quality should become worse but the limiting magnitude should become deeper, as shown by the black line. The red points show the actual locus of the “full” stacks. The blue dots show the actual locus of the “best seeing” stacks.

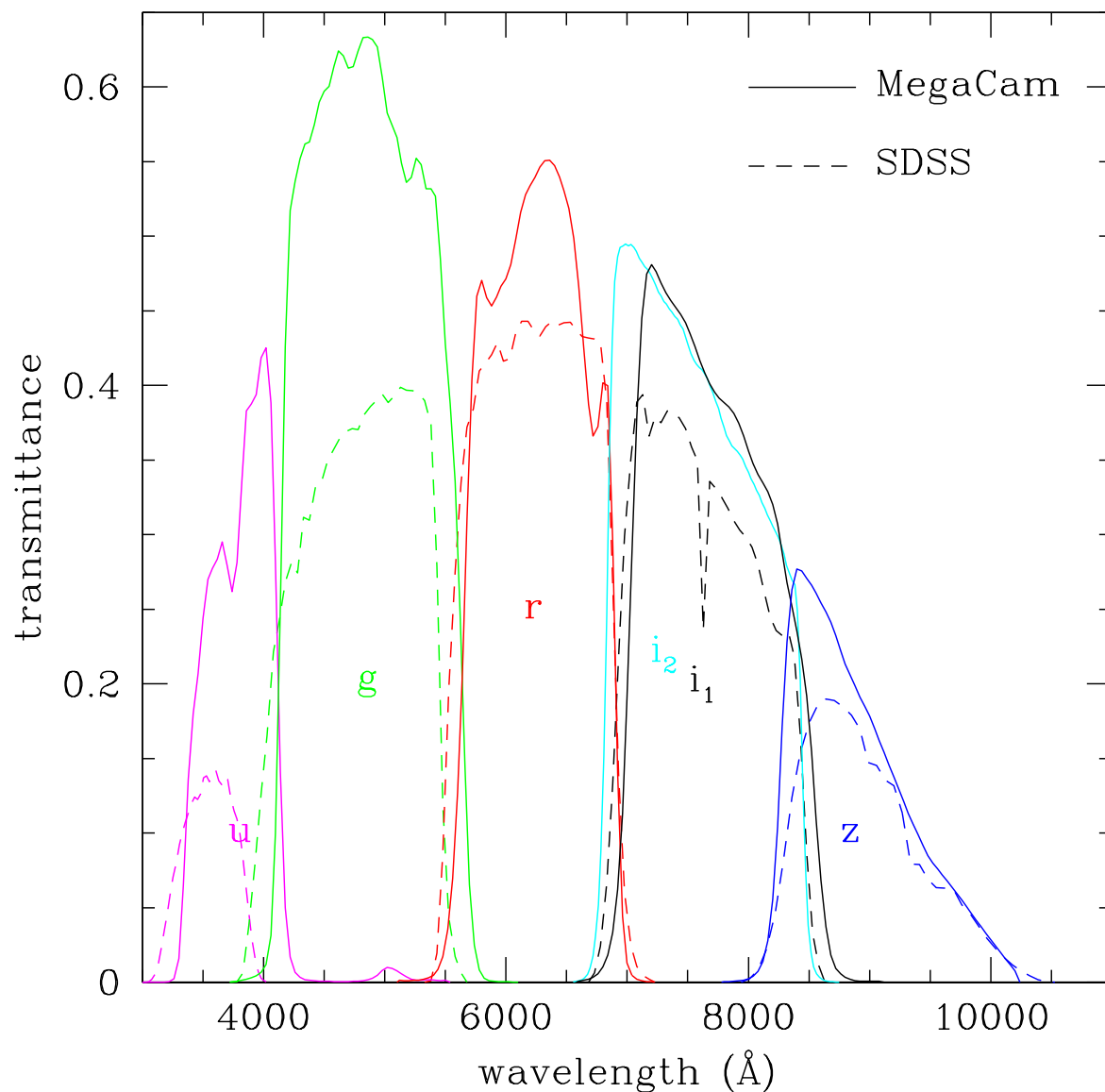


Fig. 8.— Comparing the MegaCam (solid lines) and SDSS (dashed lines) $u^*g'r'i'z'$ filter sets. The transmittance curves show the final throughput including the filters, the optics and the CCD response. There are two i' filters. The older one (CFHT filter i.MP9701) is labelled i_1 ; the newer one (CFHT filter i.MP9702) is labelled i_2 .

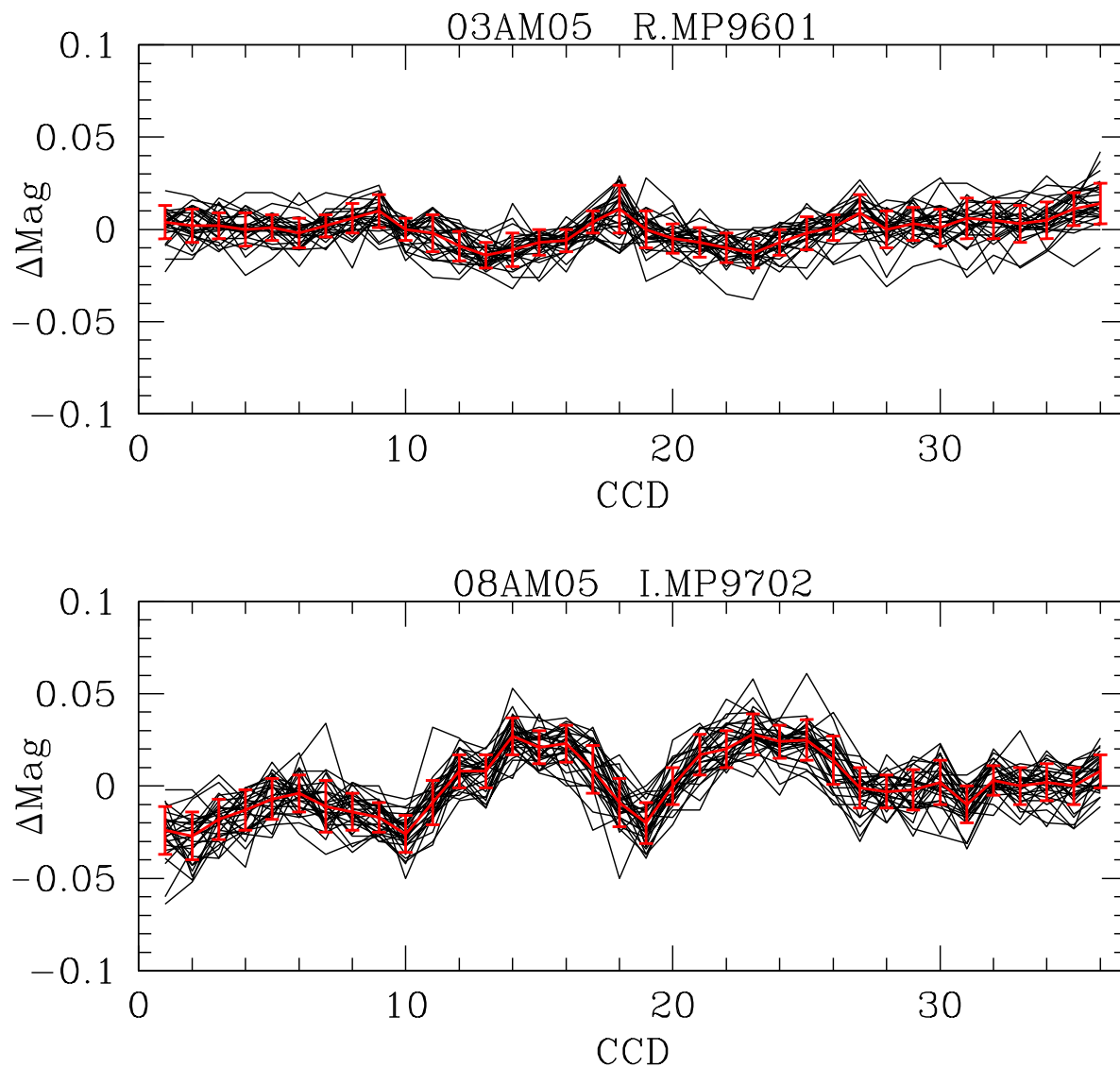


Fig. 9.— Differential zero-point variations. The black lines show the individual zero-point offsets (SDSS-Elixir) as a function of CCD number. The superimposed red line shows the median zero-point offsets. There is clearly some scatter about the median, indicated by the black lines and by the error bars (1σ). The two panels are labelled by camera run ID and filter name. The scatter in the top panel is 0.01 mags with a peak-to-peak value of 0.03 mags. The scatter in the top panel is 0.03 mags with a peak-to-peak value of 0.08 mags.

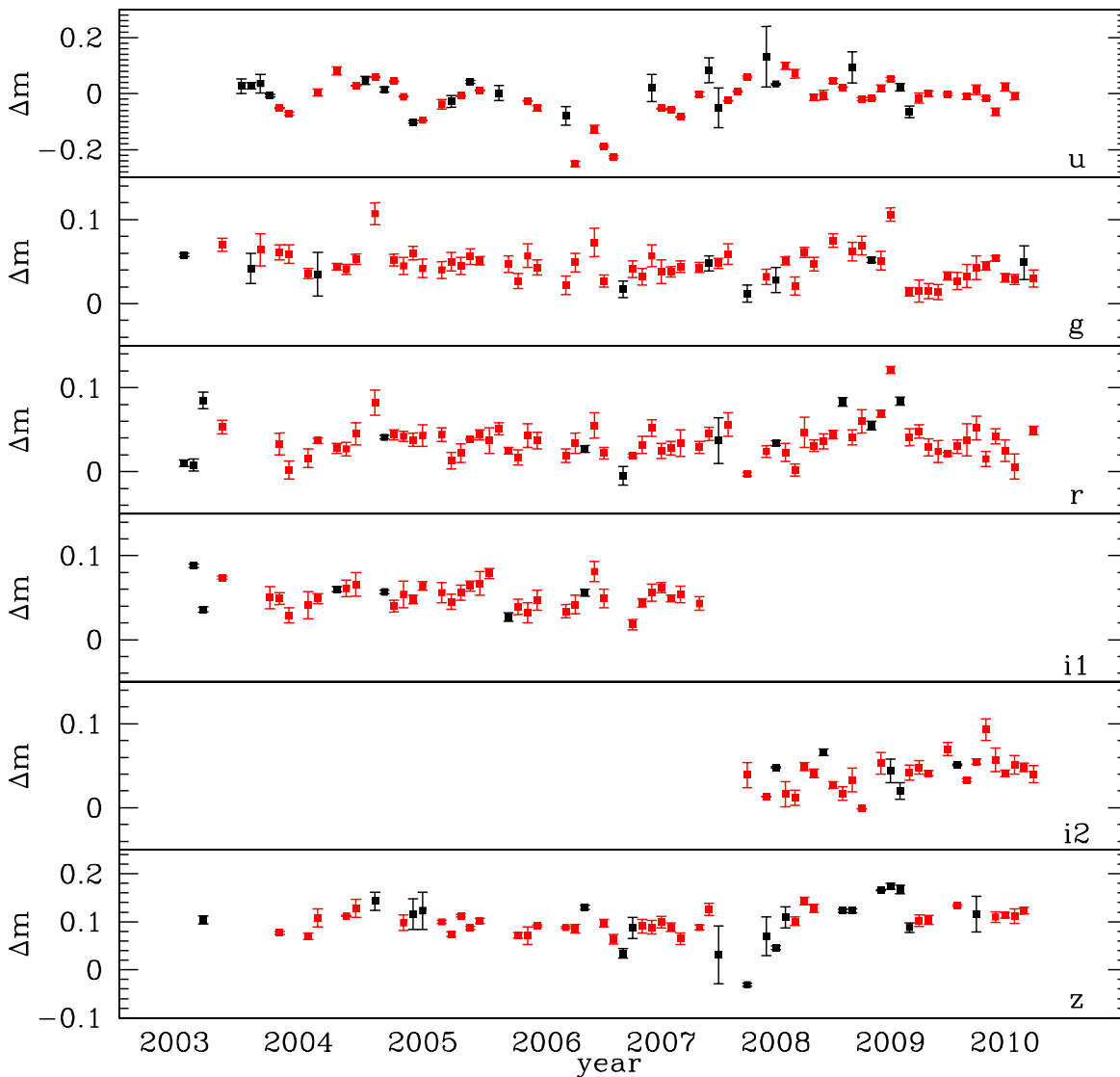


Fig. 10.— Zero-point history for the MegaCam filters. The plot shows the difference between the zero-points computed using the SDSS as a reference to zero-points computed using the the Elixir keywords. The zero-point differences are plotted as a function of time. $\Delta m = ZP_{SDSS} - ZP_{Elixir}$. Each point represents a single CRUNID. The “Excellent” cases (as discussed in the text) are shown in red. The “Marginal” case are shown in black. Note that the magnitude scales are not the same for all filters.

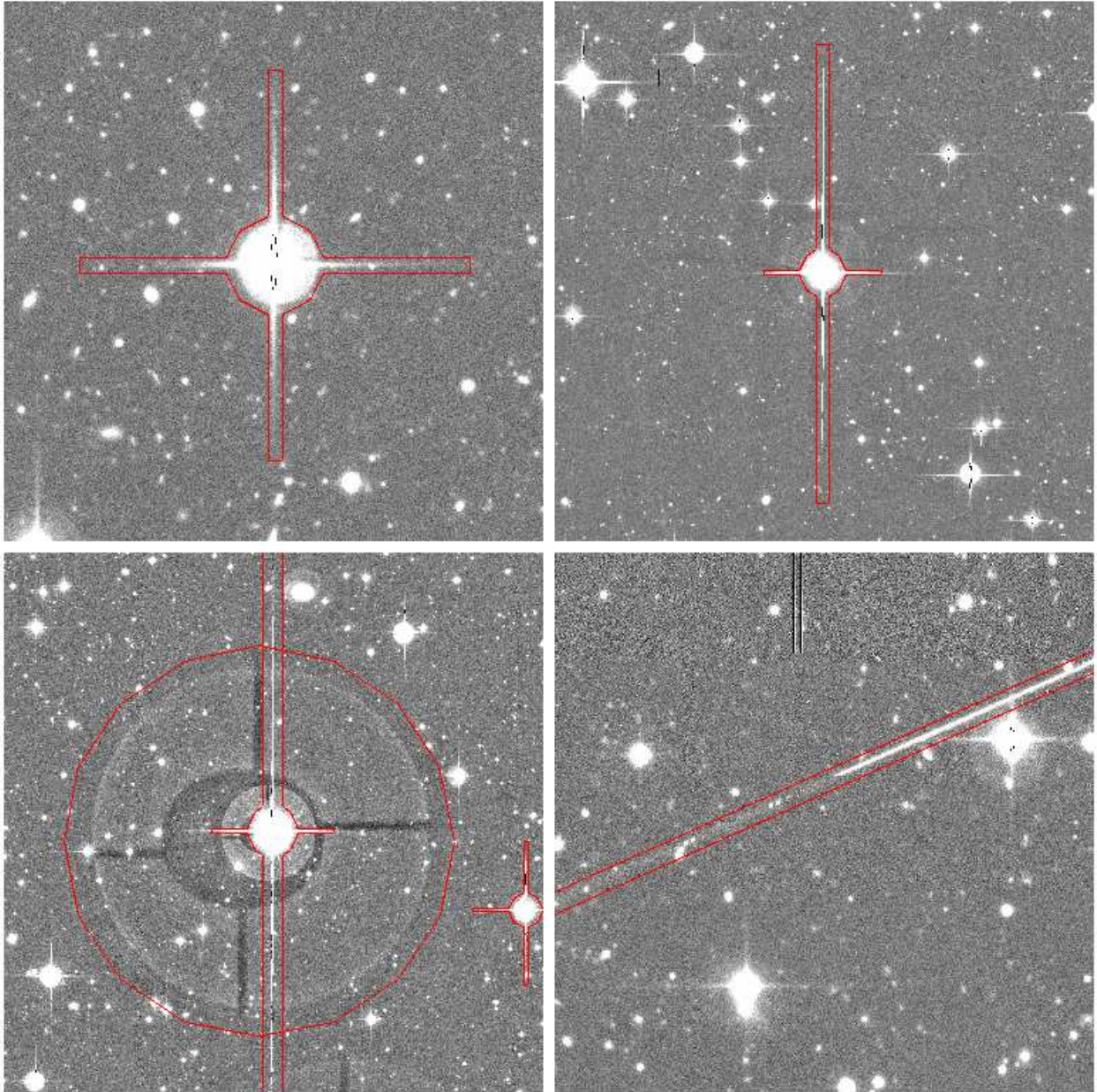


Fig. 11.— Examples of masking. The top left panel shows bright star masking, including masking of the diffraction spikes. The top right panel shows the same, but this time the mask also covers the bleed trails from the star in the y -direction. The bottom left panel shows pupil image masking; the figure shows a circular mask, which is slightly offset from the center of the star. The bottom right panel shows meteor trail masking. Note that the different panels are not at the same pixel scale.

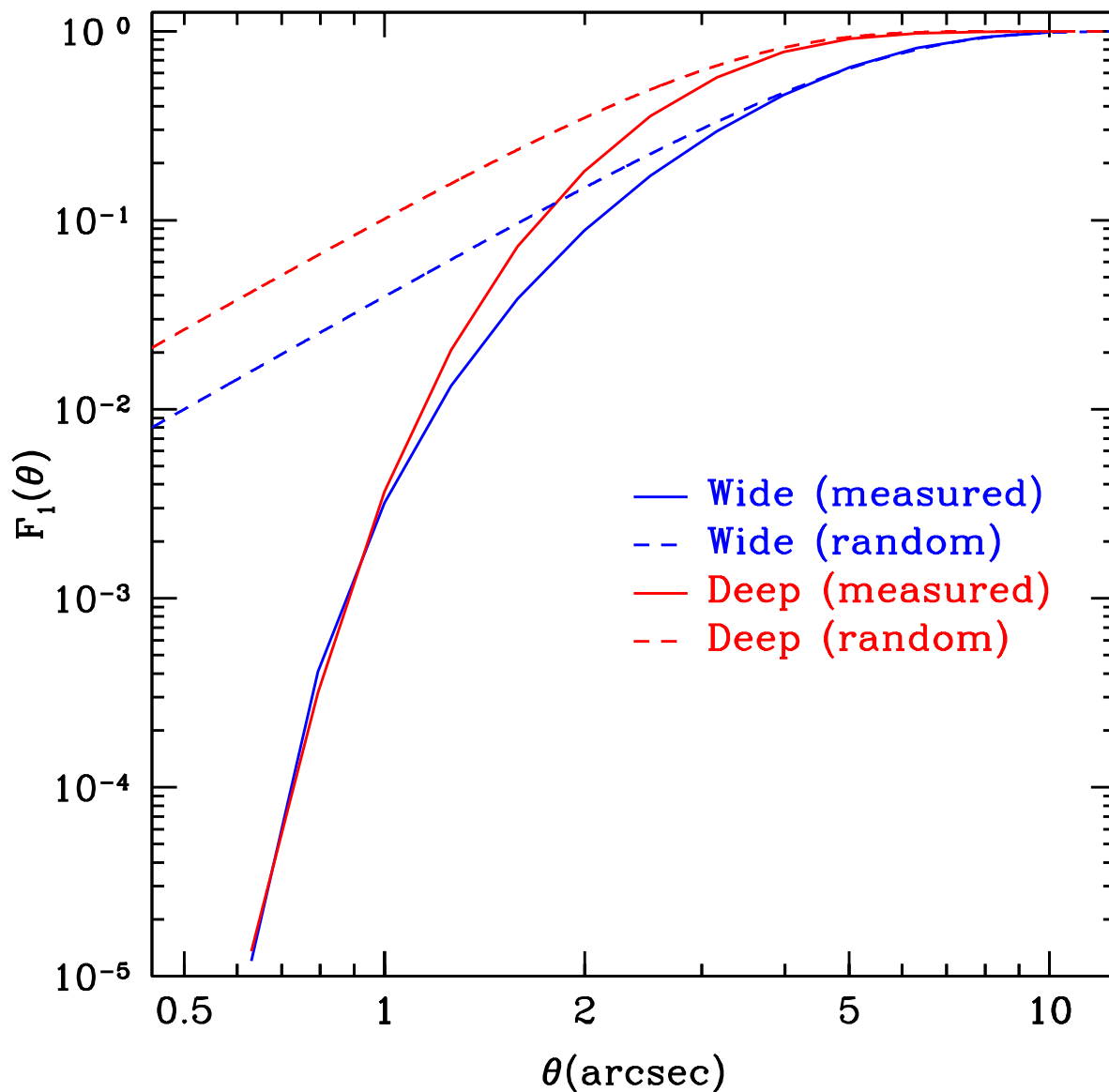


Fig. 12.— Probability of a source having a neighbour within a given radius. $F_1(\theta)$ is the fraction of sources that have at least one neighbouring source within θ arcseconds. The solid blue and red lines show the results as measured from the Wide and Deep surveys respectively. The dashed lines show the theoretical nearest neighbour fractions, assuming sources are distributed completely randomly (ignoring any galaxy clustering).

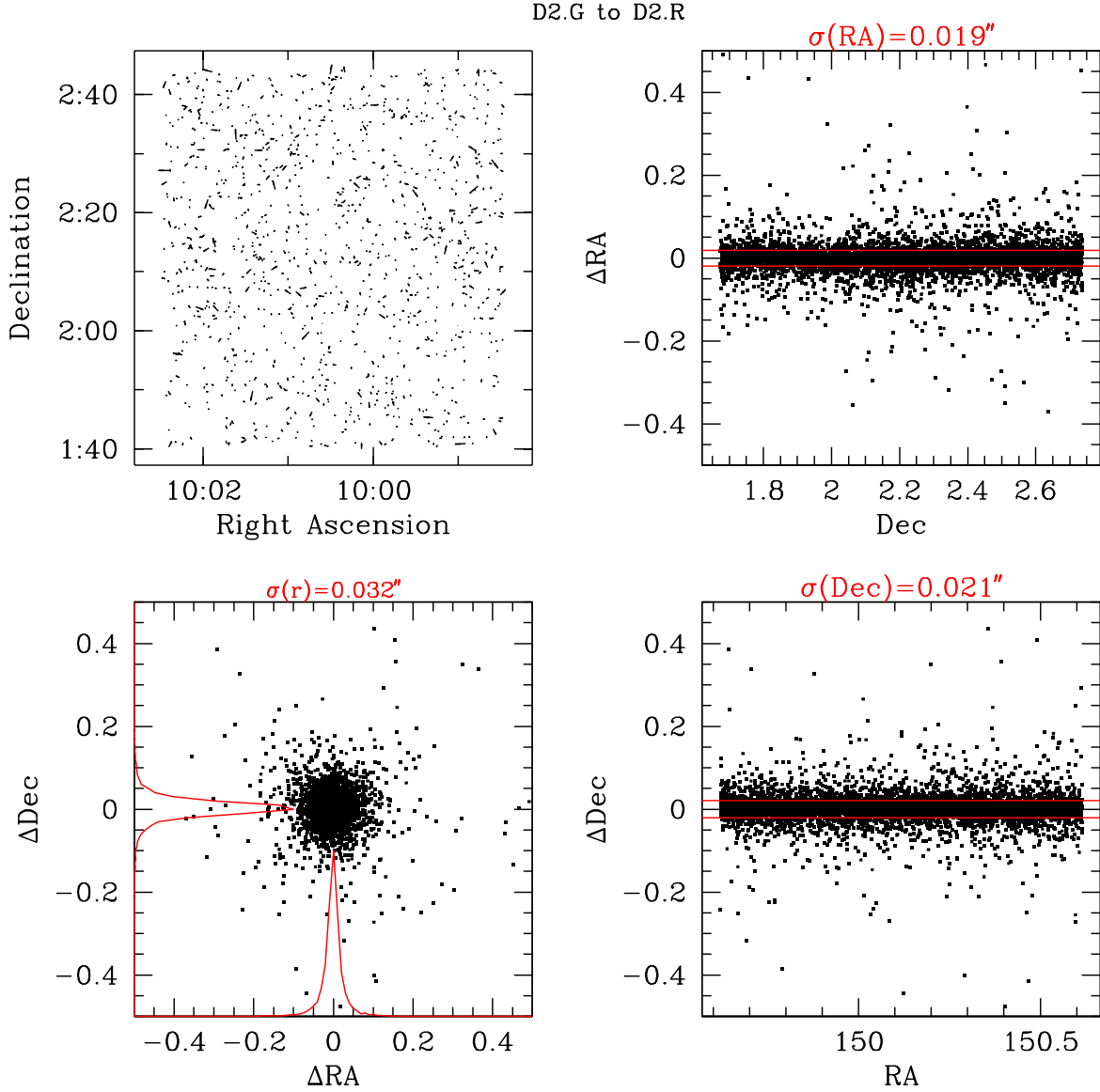


Fig. 13.— An example of internal astrometric residuals. The top left panel shows the direction and size (greatly enlarged) of the astrometric residuals as line segments. The bottom left panel shows the astrometric residuals in RA and Dec. The red histograms show the relative distribution of the residuals in both directions. The two right panels show the residuals in RA and Dec as functions of Dec and RA respectively.

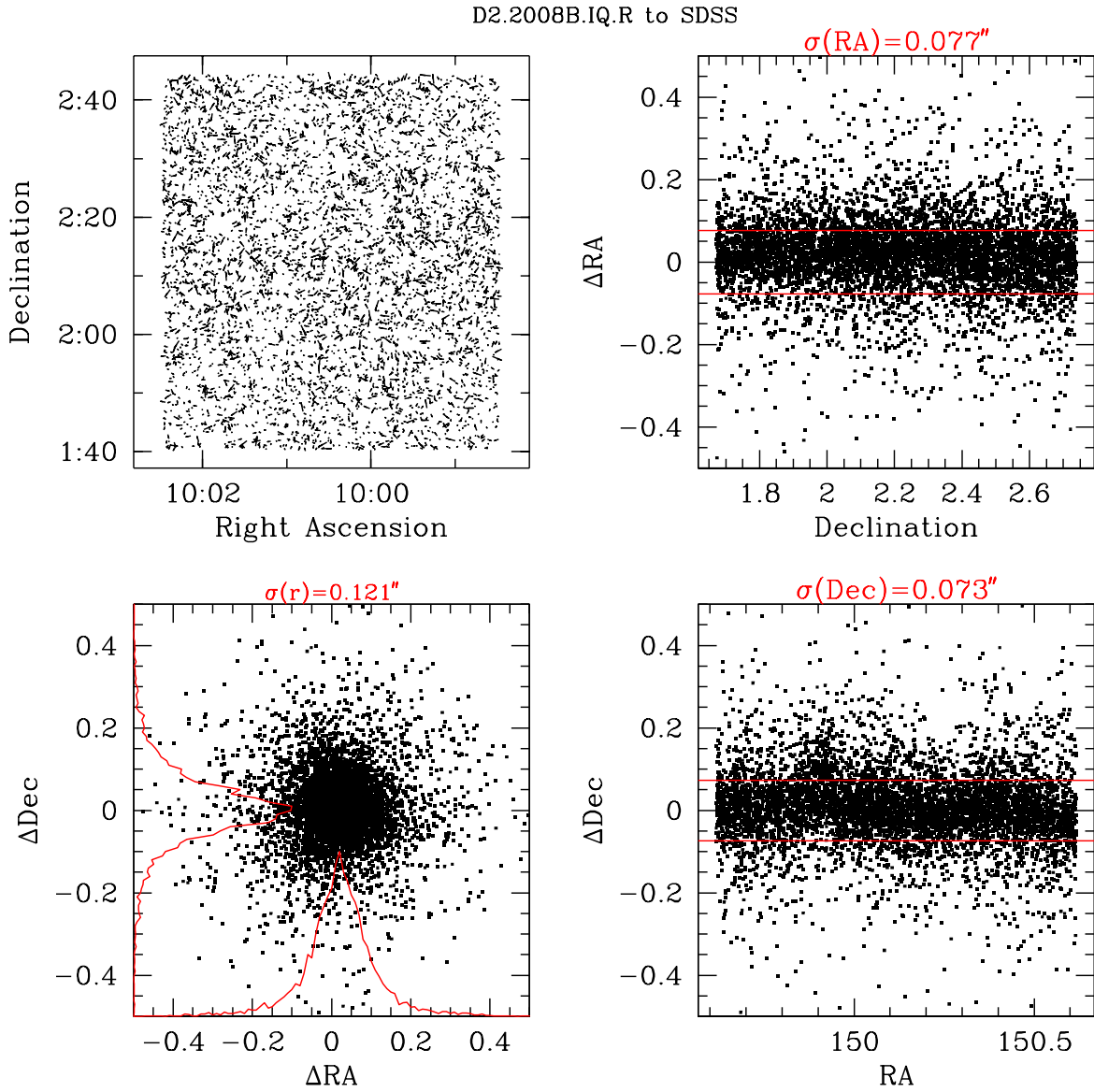


Fig. 14.— An example of external astrometric residuals with respect to the SDSS. The panels have the same meaning as in Figure 13.

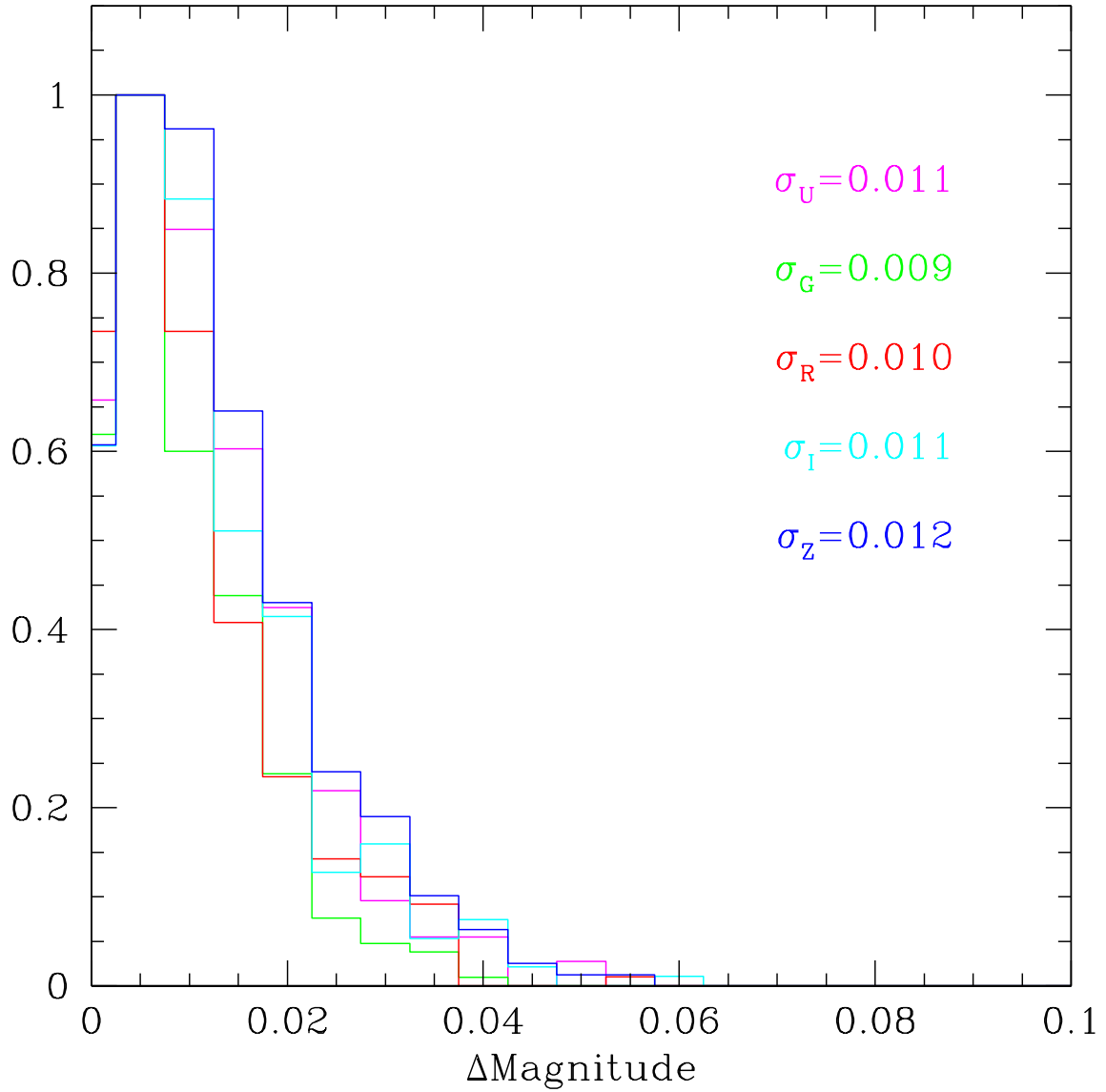


Fig. 15.— Internal photometric checks for the Wide Fields. The histograms show the photometric zero-point offsets between adjacent fields. The histograms are split by filter: the $u^*g'r'i'$ and z' filters are shown as magenta, green, red, cyan and blue histograms respectively.

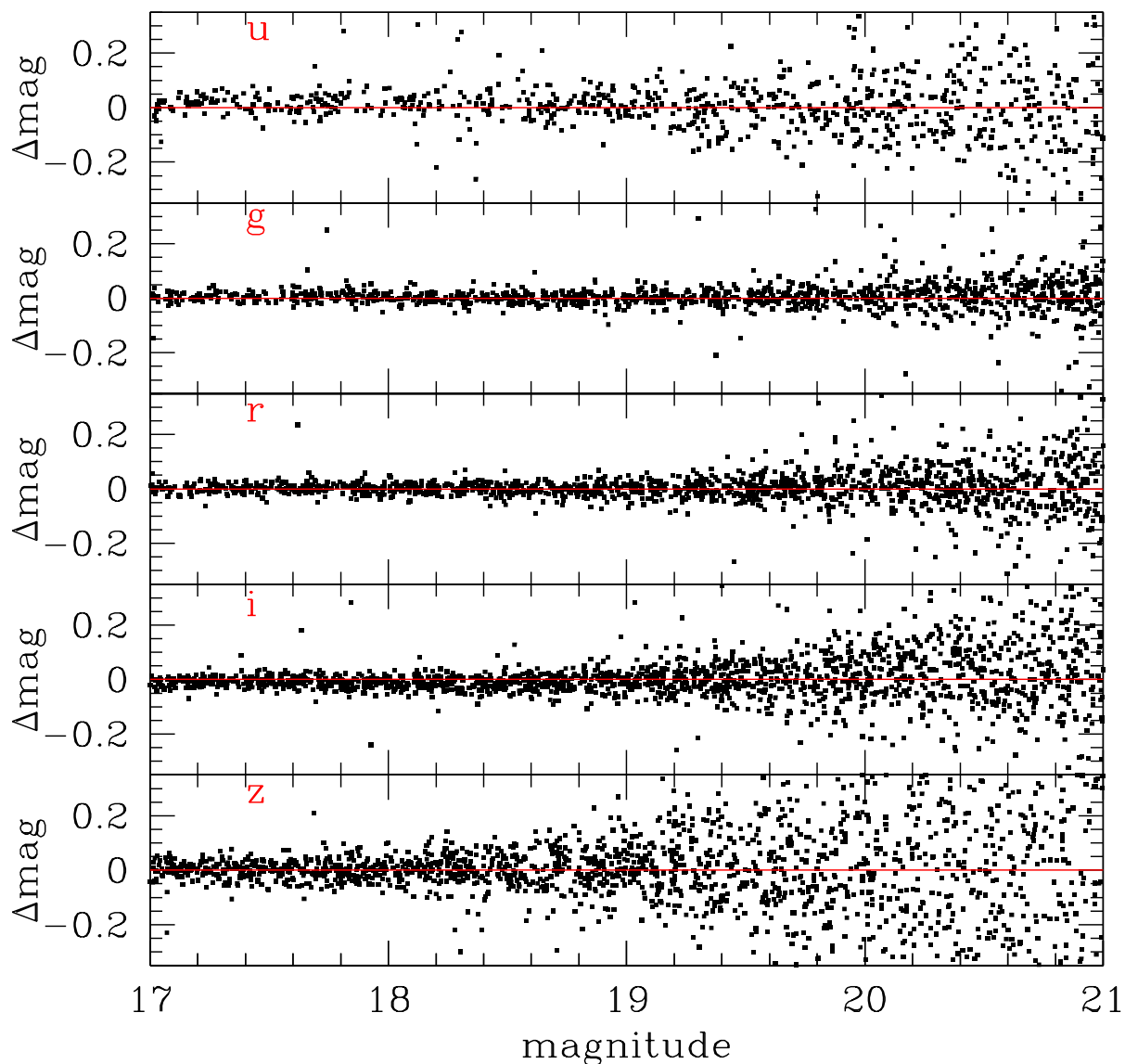


Fig. 16.— An example of a comparison of the photometry between the CFHTLS and the SDSS. The SDSS magnitudes have been transformed to the CFHTLS system. At bright magnitudes, for i' -band, there is a deviation, caused by the brightest stars saturating. In u^* -band the scatter is larger because of the larger difference between SDSS- u' and MegaCam- u^* , but the center of the distribution remains close to 0.

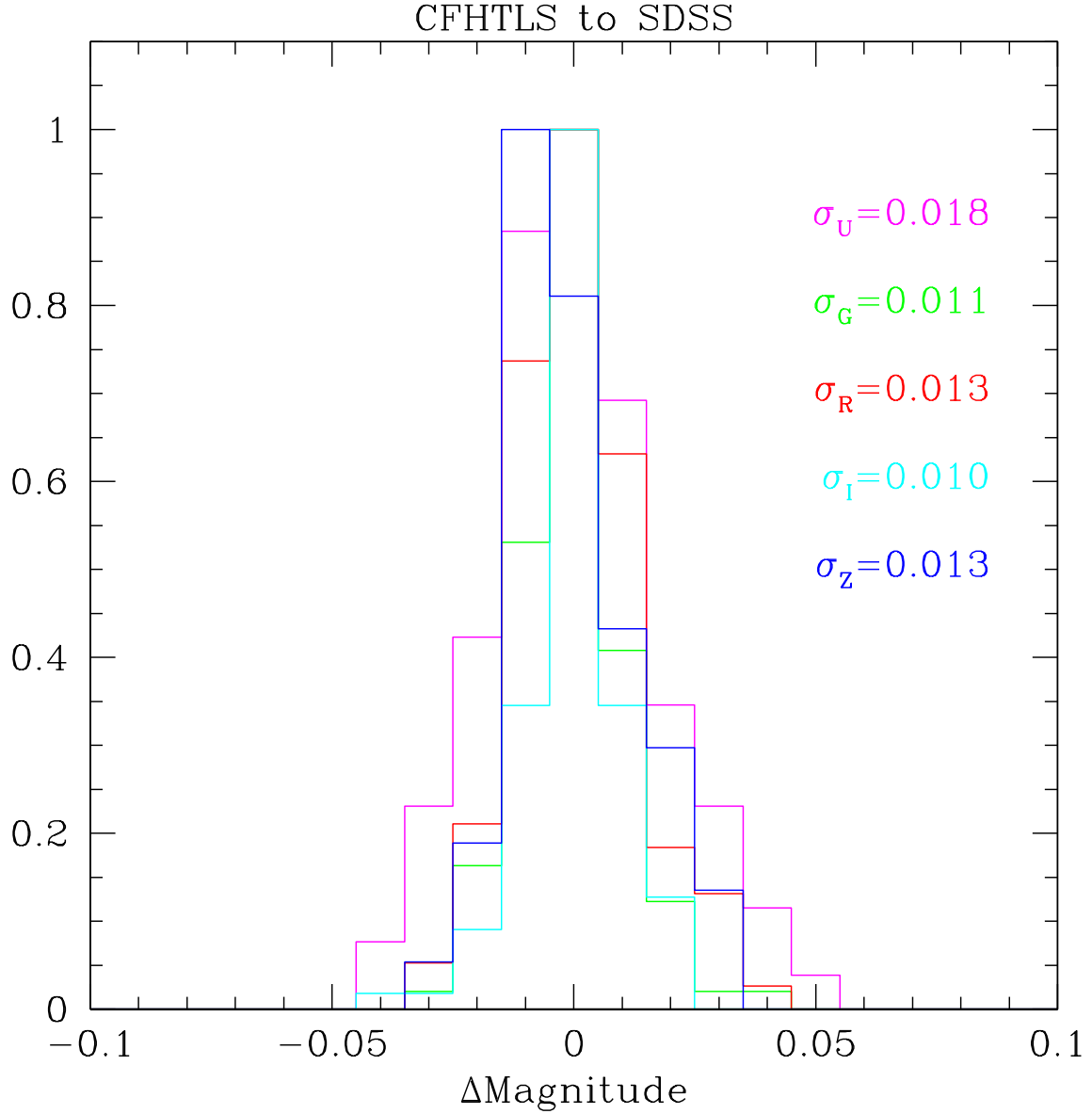


Fig. 17.— External photometric checks for the Wide Fields. The histograms show the photometric zero-point offsets between the CFHTLS and the SDSS. The histograms are split by filter as in the previous figure. The offsets are typically slightly larger than the internal photometric residuals,.

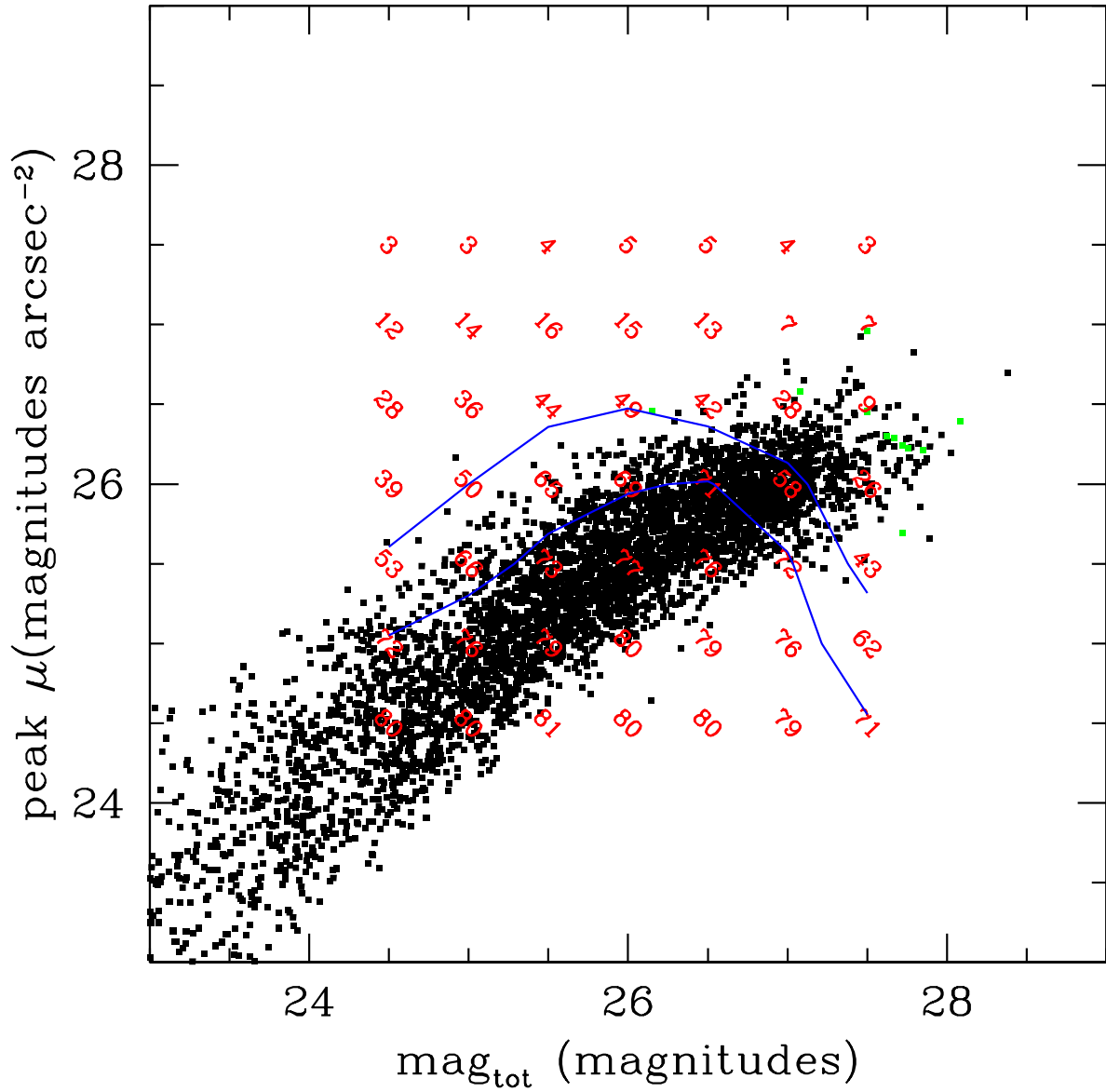


Fig. 18.— Completeness limits in magnitude and surface brightness. The black points are real objects. The green points show the false-positive detections. The red numbers show the percentage of artificial galaxies that were recovered at that magnitude/surface brightness. The blue contour lines shows the 70% and 50% completeness levels.

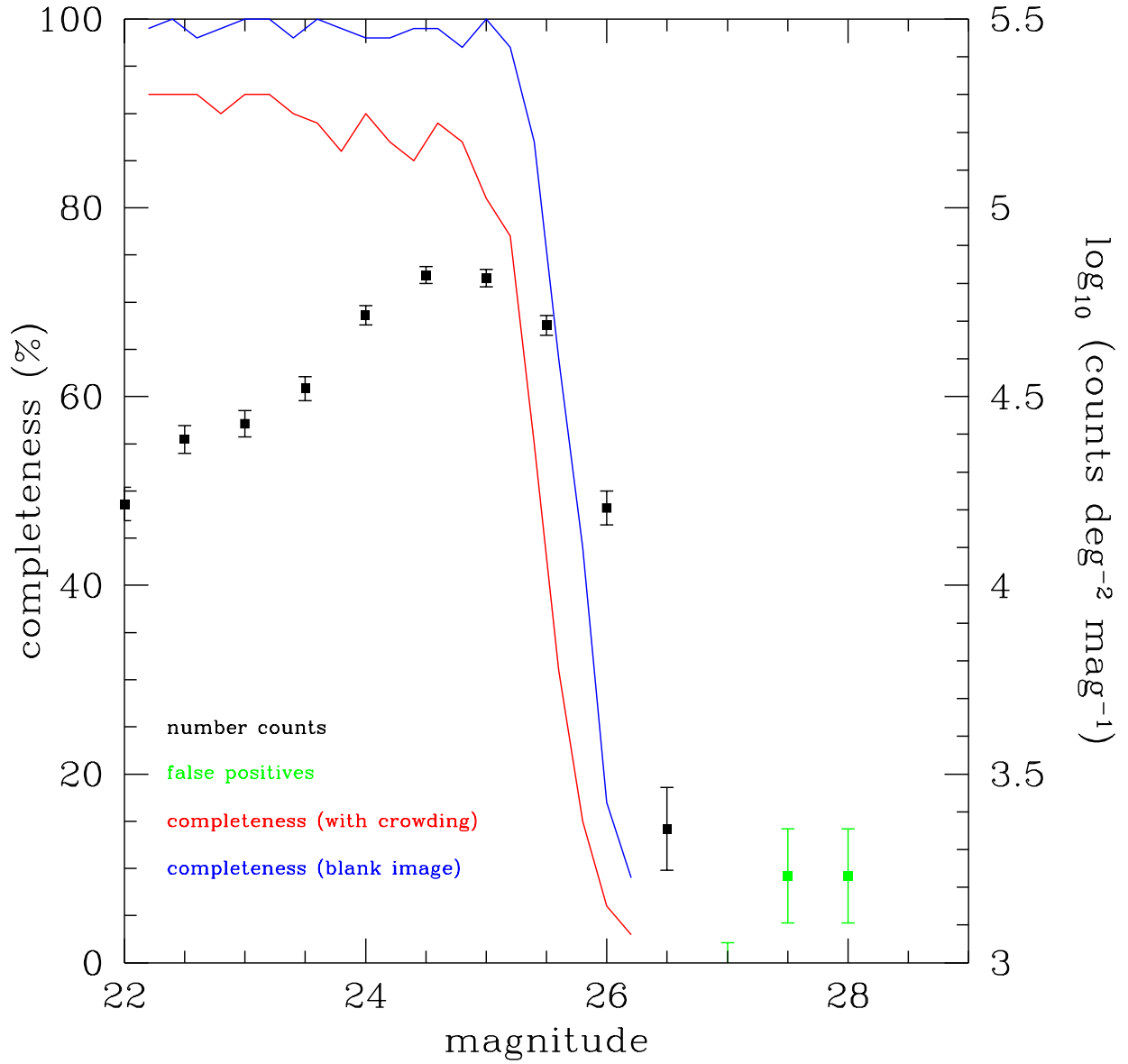


Fig. 19.— Point source completeness limits. The blue line shows the fraction of artificial point sources that can be recovered from the blank image. The red line shows the same for the original image. The black points show the number counts of real sources. The green points show the number counts for false positive detections.